

The 1997 Pan American Climate Studies Tropical Eastern Pacific Process Study. Part I: ITCZ Region*



Sandra E. Yuter and Robert A. Houze Jr.
Department of Atmospheric Sciences, University of Washington, Seattle, Washington

ABSTRACT

The Pan American Climate Studies Tropical Eastern Pacific Process Study (TEPPS) obtained a comprehensive set of observations of the structure of clouds and precipitating storms over the eastern tropical Pacific from 28 July to 6 September 1997. The TEPPS data can address a wide range of problems involving tropical oceanic clouds and precipitation. The main goal of the project was to understand why passive microwave satellite algorithms indicate an E–W gradient in the precipitation pattern in the tropical Pacific with heavier rainfall in the east while infrared satellite algorithms indicate heavier rainfall in the west. Satellite-derived precipitation estimates are based on characteristics of the vertical structure of precipitating clouds: in the case of infrared methods, cloud-top temperature, and in the case of microwave methods, the vertically integrated ice scattering and/or water absorption determined by the vertical profile of hydrometeors. The premise of the expedition was that by obtaining surface-based radar measurements of the vertical structure of precipitation where and when the differences between the infrared and microwave precipitation estimates were large, it could be determined which satellite method yielded a more accurate pattern of precipitation in the Pacific. This paper describes the types of observations obtained during TEPPS and some preliminary results.

A single, well-equipped vessel on its maiden voyage, the National Oceanic and Atmospheric Administration ship *Ronald H. Brown*, was the base for all observations. Scanning C-band Doppler radar and cloud photography documented the three-dimensional structure of clouds and precipitation in the vicinity of the ship. Upper-air soundings were obtained at ≤ 4 h intervals. Surface meteorological and oceanographic instruments and vertically pointing 915-MHz and S-band profilers characterized conditions at the ship itself. During 28.5 days in the eastern Pacific ITCZ, the shipborne radar observed echoes larger than 50 km in maximum horizontal dimension within 100-km radius of the ship 71% of the time and larger than 100 km 55% of the time. The ship spent 16 days on station at 7.8°N, 125°W and 4 days in the vicinity of Hurricane Guillermo.

Samples of surface atmospheric and oceanic data collected during the cruise illustrate the difficulty of interpreting short timescale buoy data time series in the absence of the mesoscale context provided by radar data. The ship sounding data show that the larger-scale, longer-lived convective precipitation activity and organization on timescales of days in the eastern Pacific ITCZ is closely associated with the presence of stronger southerly winds, which in turn suggests that large-scale atmospheric processes such as easterly waves or inertial stability oscillations are a regulating mechanism.

Comparison of the ship radar data, satellite IR data, and satellite microwave data shows that part of the reason why the IR and microwave-derived precipitation maps differ is that in the eastern Pacific ITCZ IR cold cloudiness resolves only a subset of the precipitation detected by microwave data. Large precipitating systems (> 100 km scale) of long duration (> 24 h; i.e., the mesoscale organized systems) were reliably associated with cold cloudiness < 235 K. Precipitating systems of shorter duration and/or smaller scale (i.e., the less-organized convection) sometimes reached 235 K and sometimes did not. Satellite microwave data generally agreed with the radar data regarding the location and areal coverage of precipitating regions larger than ~ 10 km in horizontal scale. However, the microwave algorithm examined in this study had varying degrees of skill in locating the heavier rainfall areas within rainy regions.

*JISAO Contribution Number 639.

Corresponding author address: Prof. Sandra Yuter, Atmospheric Sciences, Box 351640, University of Washington, Seattle, WA 98195-1640.

E-mail: yuter@atmos.washington.edu

In final form 11 June 1999.

©2000 American Meteorological Society

1. Introduction

The eastern tropical Pacific is a focus of research aimed at improving global circulation models (GCMs) and coupled models used to predict seasonal and interannual climate variability. The representations of

deep convection in the intertropical convergence zone (ITCZ) and of the adjoining stratus and stratocumulus regions are key to improving these models. This paper describes the Tropical Eastern Pacific Process Study (TEPPS), the first process study of the Pan American Climate Studies (PACS) program, which aims to improve knowledge and parameterization of deep and shallow oceanic clouds. TEPPS was a shipboard expedition to investigate the structure of clouds and precipitation in the open ocean within the eastern tropical Pacific ITCZ and the subtropical marine stratocumulus regions. The surface-based observations obtained during TEPPS contribute to better physical interpretation of satellite remote sensing of these regions and form a basis for more accurate validation of large-scale models.

The PACS TEPPS cruise was the first research cruise of the new National Oceanic and Atmospheric Administration (NOAA) ship *Ronald H. Brown* (Fig. 1, Table 1), which is designed to support both atmospheric and oceanic research. For the TEPPS cruise, the *Brown* was equipped with a scanning C-band Doppler radar, an upper-air sounding system, a 915-MHz wind profiler and Radio Acoustic Sounding System (RASS), an S-band profiler, and a variety of surface meteorology and upper oceanographic sensors, including 15 rainfall measurement instruments.

TEPPS was originally designed as an ITCZ experiment. A medical evacuation cut short the planned time in the ITCZ but afforded the opportunity to examine



FIG. 1. The *Brown* on station at 7.8°N, 125°W at 2130 UTC 21 Aug 1997. The variety of cloud types present during this “suppressed” period of high cloudiness included cirrus, cumulus, cumulus congestus, and a hint of part of an anvil from a cumulonimbus behind the ship. Convective overturning of the atmosphere is occurring and reaching moderate vertical extent; however, the precipitation regions are isolated and not organized on the mesoscale.

the marine stratocumulus region to the west of Mexico. Thus, two distinct types of clouds and precipitation were observed with the same suite of shipboard instruments over the course of the 49-day cruise: the deep convective regime of the ITCZ and the cloud-topped boundary layer of the marine stratocumulus region. The stratocumulus portion of the TEPPS cruise is discussed in detail in Part 2.

2. Rainfall over the open ocean

Unlike other geophysical variables such as temperature and pressure, precipitation is discrete in time and space. The lifetime of a precipitating region is related to its size, varying from tens of minutes for isolated precipitating cells to tens of hours for organized mesoscale convective systems (Chen et al. 1996; Machado et al. 1998). The frequency of occurrence of precipitating systems tends to be inversely related to size, with small showers occurring much more frequently than long-lived, 100+ km scale precipitation systems.

Continuous measurements over a multiweek period are needed in order to observe the initiation, life cycle, and environmental recovery associated with several large precipitation events. A C-band meteorological radar mounted on a ship is the only practical means of obtaining these types of observations in remote open-ocean regions and has been employed in previous open-ocean field experiments such as the Global Atmospheric Research Program Atlantic Tropical Experiment (GATE; Kuettner et al. 1974) and the Tropical Ocean and Global Atmosphere Coupled Ocean–Atmosphere Response Experiment (TOGA COARE; Webster and Lukas 1992; Godfrey et al. 1998). Shipborne volumetric radar measurements can characterize both the vertical structure and surface precipitation associated with convective cloud systems; thus, they are a cornerstone to improving understanding of precipitation processes over open-ocean regions and the central focus of TEPPS.

a. Precipitation in the ITCZ

The enhanced cloudiness and rainfall of the ITCZ are the manifestations of the upward branch of the Hadley circulation and its associated large-scale, low-level convergence. Accurate estimates of the temporal and spatial distribution of precipitation and its magnitude within the ITCZ are an important component in the diagnosis and validation of GCMs and

TABLE 1. Selected characteristics of the NOAA ship *Ronald H. Brown*.

Commissioned	19 Jul 1997
Length overall	83.5 m
Breadth	16 m
Draft	5.2 m
Displacement—Full load	3 250 tons
Displacement—Lightship	2 100 tons
Sustained speed	13 kt
Propulsion	Two 3000-HP Z-drives Lips type FS 2500-450/1510 BO
Bow thruster	One 1180-HP azimuthing jet
Dynamic positioning system	Robertson RMP ROBPOS system
Endurance	11 300 n mi at 12 kt plus 30 days on station
Accommodations (max)	59
Heights from water line	
05 level	15.85 m
04 level	13.49 m
03 level	10.97 m
02 level	8.46 m
01 level	5.94 m
Main deck	3.2 m
Navigation sensors	P-code (differential) GPI ODEC Model DSN-450 four-beam Doppler speed log

coupled models. In many regions of the world, satellite data are the only viable means regularly available to estimate precipitation since surface rain gauge observations are sparse.

The vertical structure of convection affects both the IR and microwave estimates of precipitation. Microwave brightness temperatures respond directly to the vertically integrated liquid and ice hydrometeor content of the cloud, and thus only indirectly to surface rainfall (Wilheit 1986; Smith et al. 1992; Kummerow 1998). Satellite IR brightness temperatures are a measure of cloud-top height, which has an indirect, purely empirical relation to surface rainfall (Arkin and Meisner 1987).

Current satellite-based precipitation estimates derived from microwave and infrared data show reasonable agreement in some regions but exhibit large discrepancies in others (Spencer 1993; Janowiak et al. 1995; Xie and Arkin 1996). The average June–August precipitation for 1986–95, over the tropical Pacific derived from microwave sounder data (Spencer 1993 with “Limb90” correction) and from Geostationary Operational Environmental Satellite IR data (Arkin and Meisner 1987) are shown in Fig. 2. Particularly notable is that the E–W gradient of precipitation is reversed in the region from 160°E to 120°W depending on which satellite instrument is used to derive the estimate. While the magnitude of the mean rainfall in the western Pacific is similar between the IR and microwave estimates, in the eastern Pacific ITCZ, away from the monsoonal influence of the American landmasses, the microwave-derived estimate is over twice that of the IR-derived estimate (Table 2). There must be an underlying physical reason for this difference. One current hypothesis is that eastern Pacific storms are associated on average with a larger magnitude of vertically integrated ice scattering than storms over the western Pacific warm pool (E. Smith 1999, personal communication). Apart from such meteorological differences, the assumptions of the algorithms used for estimating rain from one or both data types may be tuned better for one region than the other.

TEPPS aimed to understand the physical reasons for the discrepancy between the microwave- versus IR-derived precipitation patterns and to estimate rainfall independently using surface-based measurements. TOGA COARE provided such a dataset for the western end of the tropical Pacific (point W in Fig. 2c). As a counterpoint to TOGA COARE, TEPPS collected data near point E in the eastern Pacific (Fig. 2c). The study was conducted at a location and at a time of year (August) where and when the differences between the microwave- and infrared-based precipitation estimates are largest, in order to obtain a strong signal of the factors responsible for the discrepancies. During this

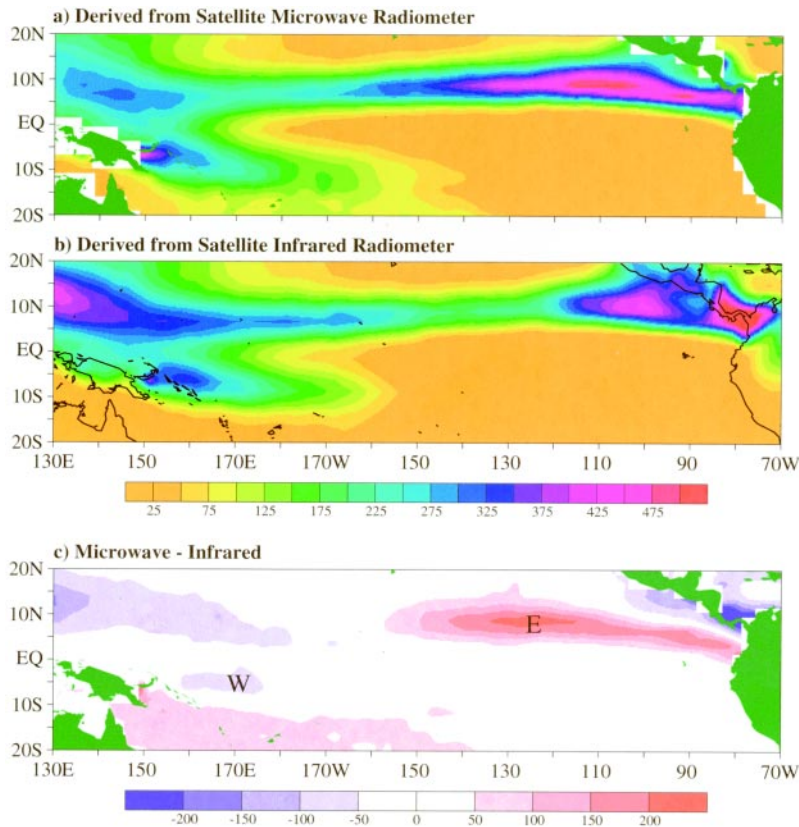


FIG. 2. Comparison of average Jun–Aug precipitation over the Tropics inferred from satellite microwave radiometer data and satellite infrared radiometer data. (a) Jun–Aug average microwave sounding unit (MSU) derived precipitation for years (1986–95) using the method of Spencer (1993) with “Limb90” correction. (b) Jun–Aug average GOES Precipitation Index (Arkin and Meisner 1987) derived from GOES IR data from 1986 to 1995. (c) Difference between microwave and infrared-derived estimates. The “W” indicates where TOGA COARE data was collected; “E” indicates where TEPPS data was gathered. (Figure courtesy of T. Mitchell, JISAO.)

time of year, the meridional SST gradient and southerly wind are both strong in the eastern Pacific (Mitchell and Wallace 1992). The SST gradient provides a strong large-scale forcing for the precipitation in the eastern Pacific. This characteristic is another possible physical difference between the east and west Pacific, where large-scale horizontal gradients of SST are absent.

b. Sampling during the El Niño–Southern Oscillation

The tendency for air to overturn (i.e., for convection and hence precipitation to occur) and the depth of that overturning are related to the vertical stability of the atmosphere and especially to the temperature and moisture characteristics of the air near the surface. The SST con-

strains the maximum temperature and humidity of the atmosphere just above the ocean surface. As a consequence, the energy available for convection is likely to be less in regions where the SST is lower. The TEPPS cruise occurred during the El Niño–Southern Oscillation (ENSO) warm event of 1997. Table 3 shows the average sea surface temperature (SST) in the region of the TEPPS on-station sampling for 1996–98. During August 1997 when the shipborne observations were obtained, SSTs were 1°C warmer than during the non-ENSO year of 1996. The eastern Pacific environment associated with the warmer SSTs during the ENSO-year TEPPS cruise was therefore probably more convectively active than during a non-ENSO year. The location of the eastern Pacific ITCZ also shifted southward from its climatological position during the 1997 ENSO year. To compensate for this effect, we shifted the ship’s on-station location southward from the originally planned location at 10°N.

3. Ship-based observations

The *Brown* was equipped with standard surface atmospheric and upper-oceanographic instruments, an upper-air sounding system, and several supplemental sensors brought onboard specifically for the TEPPS cruise, including a C-band Doppler radar, a 915-MHz profiler and RASS, an S-band profiler, and several additional rain measurement instruments (Fig. 3). The intensive, multi-sensor observational strategy from a single ship

TABLE 2. Average Jun–Jul–Aug monthly rainfall (1986–95) for selected $2.5^\circ \times 2.5^\circ$ boxes in eastern and western Pacific in mm month⁻¹. (Data courtesy of T. Mitchell, JISAO.)

	Microwave-derived estimate	IR-derived estimate
Western Pacific (6.2°S, 168.75°W)	209	268
Eastern Pacific (8.75°N, 126.25°W)	458	219

in TEPPS permitted collection of a highly integrated set of volumetric and in situ atmospheric and upper-ocean observations.

a. Ship track

The NOAA ship *Ronald H. Brown* was commissioned at Charleston, South Carolina, on 19 July 1997 and left Charleston on 21 July for the PACS TEPPS cruise. Figure 4 shows the TEPPS ship track. The transit time in the Atlantic was needed to finish various details on the ship's data systems, and data were not systematically collected and recorded until the ship reached the Pacific Ocean on 28 July 1997. The type of meteorological regime sampled during each of the legs in the Pacific is given in Table 4. During part of the transit across the Pacific from Panama, the ship spent several days in and out of rainbands associated with Hurricane Guillermo (Fig. 5), which reached peak intensity at 0000 UTC 5 August 1997 with a central pressure minima of 919 hPa and maximum wind speeds of $\sim 70 \text{ m s}^{-1}$ (M. Mayfield 1998, personal communication). The ship stopped at its on-station location, 7.8°N, 125°W [30 km south of the 8°N, 125°W Tropical Atmosphere–Ocean (TAO) buoy] on 0345 UTC 8 August 1997, and remained there until 2120 UTC on 23 August 1997, when a medical emergency forced the ship to leave the ITCZ and evacuate to San Diego, California.

For the stratocumulus portion of the cruise, the ship followed a polygon track (Fig. 4, dashed line) starting from and ending at San Diego. The observational strategies were modified from those used in the ITCZ to optimize data collection in a shallow stratus cloud regime (see Part II).

b. C-band radar

To understand the difference between the satellite IR and microwave precipitation patterns, TEPPS aimed to characterize the vertical structure of precipitation. The C-band Doppler radar on the *Brown* (Table 5) mapped reflectivity and radial velocity in

TABLE 3. Average SST measurements °C for the region of the TEPPS on-station observations. The shipboard average is for the on-station period (8–23 Aug 1997). The buoy measurements are averaged over the entire month.

Platform	Location	Aug 1996	Aug 1997	Aug 1998
WHOI IMET buoy	10°N, 125°W	NA	28.6	28.1
TAO buoy	8°N, 125°W	28.0	29.0	NA
NOAA ship <i>Brown</i>	7.8°N, 125°W	NA	29.0	NA

three-dimensional volumes surrounding the ship. The reflectivity data provide information on the vertical and horizontal distribution of precipitation-sized ice and rain particles. Low-level reflectivity can be used to estimate surface rainfall. The radial velocity volumes provide information on the air motions within the precipitating cloud. In combination, the reflectivity and radial velocity data yield information on the joint variation of microphysical and dynamical pro-

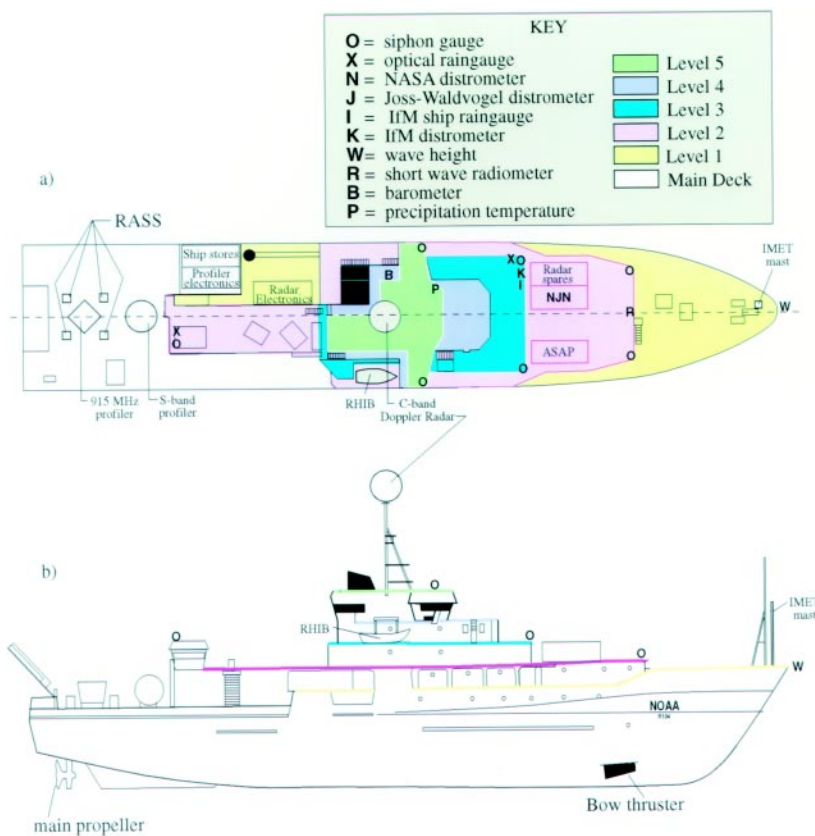


FIG. 3. Positioning of meteorological instrumentation on the *Brown* for PACS TEPPS. (a) Top view and (b) side view.

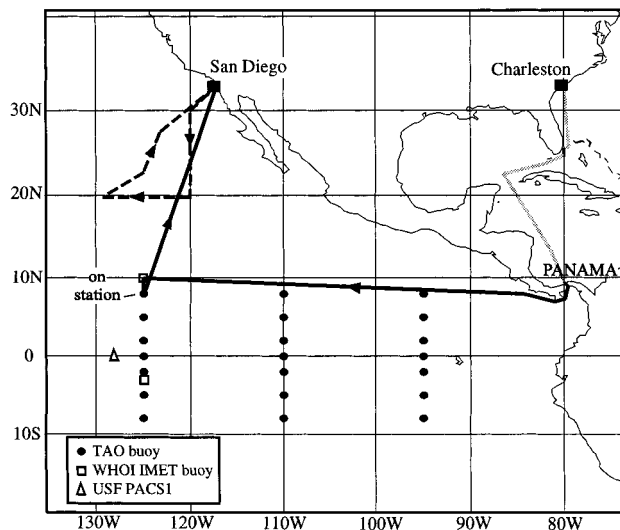


FIG. 4. Ship track of the *Brown* during the TEPPS cruise. Solid track indicates ITCZ region study and dashed track indicates marine stratocumulus region. Gray track indicates transits when data were not collected. The ship stopped at the WHOI buoy at 10°N, 125°W and the TAO buoy at 8°N, 125°W to make repairs to buoy instrumentation prior to going on station at 7.8°N, 125°W.

cesses, which produce the observed precipitation structures. The antenna, pedestal, transmitter, and antenna controller of the Massachusetts Institute of Technology C-band radar used in PACS TEPPS were the same instrumentation as used in TOGA COARE when the radar was on the NOAA ship *Vickers*. The signal processor and computer system were upgraded prior to the TEPPS cruise and were optimized for research performance by SIGMET Inc. during a shakedown cruise on 15 July 1997. Radar calibrations were performed three times while on station in the ITCZ using tethered and free-floating, balloon-borne metallic spheres (G. Gray 1997, personal communication).

Table 6 indicates the radar scanning strategy. A low-elevation surveillance scan extending to 240-km range was obtained every 15 min. The low elevation angle surveillance scans provide a larger-scale qualitative context for the volumetric data. In the time interval between surveillance

scans, two three-dimensional volume scans extending to 100-km range were obtained, each taking 6–7 min to complete. These two successive volume scans consisted of interleaved elevation angles in order to maximize the resolution of the radar data when combined statistically over the 15-min period while keeping the length of an individual volume scan to ~6–7 min in duration. In this way, the degree of storm evolution during the collection of a single volume should be small enough so that cross sections of a single volume could be viewed as a snapshot.

To facilitate analysis, the raw polar radar data were processed in polar coordinates to correct calibration, remove noise and spurious echoes from sea clutter, and then interpolated to a rectangular Cartesian grid centered on the ship's position using National Center for Atmospheric Research (NCAR) REORDER software. The volume scans were interpolated to a 202 km × 202 km × 19 km three-dimensional grid with a horizontal resolution of 2 km and a vertical resolution of 1 km. The surveillance scans were interpolated to a 484 km × 484 km two-dimensional grid centered at 0.5-km altitude with a horizontal resolution of 4 km. The former are similar in resolution to reflectivity products produced from the TOGA COARE shipboard data (Short et al. 1997) and the latter are similar in resolution to products produced from the GATE shipboard radar data (Hudlow 1979).

TABLE 4. Meteorological regimes sampled.

Regime	Description	Begin time	End time	No. of days
ITCZ	Transit Panama to on station	1200 UTC 28 Jul 1997	0300 UTC 8 Aug 1997	10.6
ITCZ	Vicinity of Hurricane Guillermo	1500 UTC 2 Aug 1997	1400 UTC 6 Aug 1997	4
ITCZ	On station	0300 UTC 8 Aug 1997	2100 UTC 23 Aug 1997	15.8
ITCZ	Portion of transit to San Diego	2100 UTC 23 Aug 1997	0000 UTC 26 Aug 1997	2.1
Subtropics	Portion of transit to San Diego	0000 UTC 26 Aug 1997	1900 UTC 28 Aug 1997	2.8
Sc region	Sc leg	0300 UTC 29 Aug 1997	1300 UTC 6 Sep 1997	8.5

Since precipitating convective clouds are central to TEPPS objectives, it is useful to sort the radar data relative to an index of convective activity. The C-band radar indicated the spatial scale of precipitating regions. The lowest elevation scans of shipborne radar data were examined for reflectivity echoes ≥ 20 dBZ. The longest dimension (L) of the *largest* contiguous echo in a given scan with some portion of the echo within 100 km of the ship was assigned to one of the following categories: $L < 2$ km, $2 \text{ km} \leq L < 10$ km, $10 \text{ km} \leq L < 50$ km, $50 \text{ km} \leq L < 100$ km, or $L \leq 100$ km. The largest dimension of the largest radar echo could be a straight line or follow the arc of a storm depending on the shape of the reflectivity pattern.

At any one time there was usually a spectrum of scales of echo present. The largest contiguous echo was assumed to indicate the highest degree of mesoscale organization that could be supported by the characteristics of the atmosphere in the vicinity of the ship. The scale L was determined from hourly samples of radar data. The proportion of hours while on station (7.8°N , 125°W) of each of the radar convective activity categories is shown in Table 7a. Precipitating systems with $L \geq 50$ km occurred 66% of the time. Systems with $L \geq 100$ km occurred 49% of the time. Hourly periods during which the largest contiguous echoes were less than 2 km in horizontal scale occurred only 6% of the time. Over the entire eastern Pacific ITCZ leg (Fig. 4), the shipborne radar observed contiguous echos larger than 50 km 71% of the time and larger than 100 km 55% of the time (Table 7b).

c. Surface rainfall and drop-size measurements

Estimation of surface rainfall rates from TEPPS ship radar data requires an empirical relation between reflectivity (Z) and rain rate (R) for the eastern Pacific ITCZ. With a single radar and no outlying rain gauges, the only way to obtain a Z - R relation is from drop-size measurements. Surface-based measurements of drop-size distribution are made with a disdrometer (e.g., Joss and Waldvogel 1967), which determines the size distribution (number of counts in each of several size categories) electronically. Difficulties in making

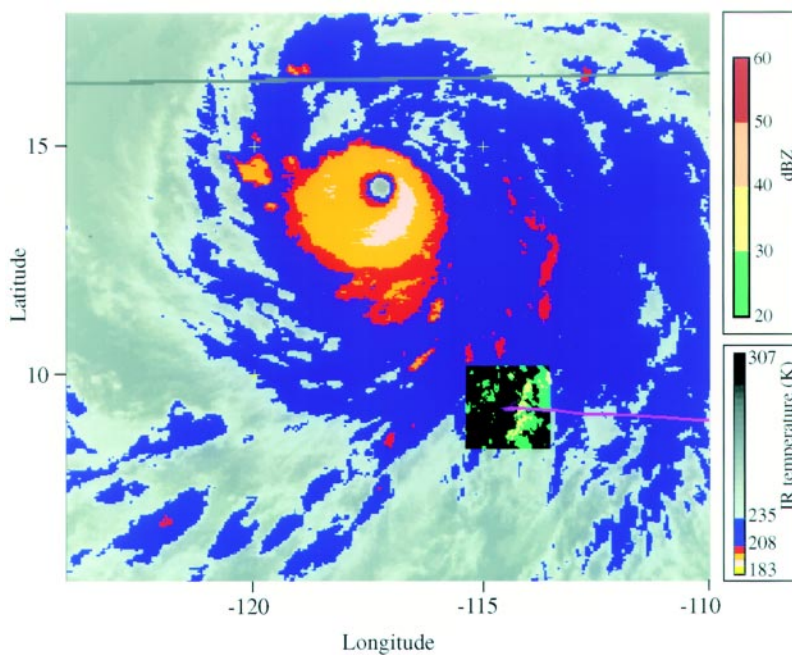


FIG. 5. Infrared satellite data from 2100 UTC 4 Aug 1997 showing Hurricane Guillermo with the ship track from the last 12 h and low-level radar data from 2145 UTC superimposed. The ship was within the inflow region of the hurricane and has just crossed through a rainband.

disdrometer measurements from shipboard are well known (Austin and Geotis 1980). In particular, vibration on the ship can lead to errors particularly at small drop sizes. The design of disdrometers for use at sea is an active area of research (Grossklaus et al. 1998; Nystuen 1999), but this work is still experimental. To address these problems, several types of disdrometers were deployed for intercomparison and steps were taken to reduce the influence of ship-induced vibration. The disdrometers deployed were a Joss-Waldvogel (JW) disdrometer (Joss and Waldvogel 1967), two pizeoelectric disdrometers (Nystuen et al. 1994), and an Institute für Meereskunde (IfM) optical disdrometer (Grossklaus et al. 1998). The latter was designed specifically for use on board ships. In addition to these automatic instruments, measurements of drop-size distribution were made manually using water-sensitive dye on filter paper (Rinehart 1995). Although the filter paper measurements are laborious to obtain and analyze, and they cannot be obtained at high time resolution, they provide an independent check of the disdrometer data and are not subject to electronic noise or vibration.

Despite the known problems with rain measurement from ships, such measurements are often the only data available. The independent measurement by rain

TABLE 5. Characteristics of MIT C-band radar on the *Brown* during the TEPPS cruise.

Model	Modified Enterprise WSR-74C
Wavelength	5.37 cm
Peak transmit power	170 kW
Pulse duration	1 ms
Minimum detectable signal	-109 dBm
Antenna gain	40.5 dB
Post repetition frequency	300–1200 Hz
Polarization	Horizontal
Beamwidth (3 dB)	1.54°
Radome	12' diameter, six gore fiberglass lamination
Stabilization	Honeywell Inertial Navigation Unit and SIGMET software
Elevation range	-10° to 65°
Doppler	Pseudocoherent with phase-locking COHO
Nyquist velocity	13.4 m s ⁻¹ at 1000 PRF
Signal processor products	dBZ (total), radial velocity, width
Data processing	SIGMET DSP and IRIX version 6.05 software
Height of feedhorn above sea level	25.56 m

gauges of rain rate at high time resolution and rainfall accumulation aids in assessing how well the disdrometers performed at sea in comparison to similar multi-instrument configurations on land (e.g., F. Bradley 1996, personal communication; Nystuen 1999). Several R. M. Young siphon gauges were used to measure rainfall accumulations, and indirectly rainfall rate. Rainfall rate was directly measured by Scientific Technology Inc. optical rain gauges (Wang et al. 1979) and an IM ship rain gauge (Hasse et al. 1998), the latter designed specifically for use on moving ships.

Skaar (1955) and Austin and Geotis (1980) have shown that the amount of rain measured on ship is primarily a function of location and hence exposure of the instrument. To address errors related to differ-

ent exposures, the rain instrumentation was distributed over the ship. The variation of precipitation measurement as a function of instrumentation type in open sea conditions was studied by clustering several types of instruments, including all the disdrometers, near the port-side 03 (03P) level (Fig. 3).

The siphon gauges and optical rain gauges used the same datalogger as the surface meteorological sensors and were logged at 10-s intervals. The data from the disdrometers and ship rain gauge were logged at 1-min intervals. The rain instrumentation was calibrated according to manufacturer specifications prior to and when applicable during the cruise.

Detailed analysis of the effect of location and wind speed on rain catchment, raindrop spectra, and application of reflectivity to rainfall relations to the radar data to produce rain maps will be the subject of subsequent papers. However, without converting to rainfall rates, radar reflectivity data are useful in qualitatively addressing many aspects of the PACS TEPPS objectives. For the purposes of this paper, the radar data will be discussed in terms of the observed reflectivities rather than derived rain rates.

d. Upper-air soundings

A total of 251 rawinsondes were successfully launched during the Pacific Ocean segment of the PACS TEPPS cruise. The schedule for sounding launches is provided in Table 8. During the ITCZ portion of the cruise, sondes were launched every 4 h. Sondes were launched every 2 h during our traverse through a mesoscale convective system during the first portion of the transit from on station to San Diego. The upper-air observations from the ship made at 0000 and 1200 UTC were transmitted via the Shipboard Environmental (data) Acquisition System (SEAS) to

TABLE 6. ITCZ radar scan strategy.

Scan name	Gate spacing (m)	PRF (Hz)	Usable range (km)	Scan rate (deg s ⁻¹)	Elevation angles in degrees
Surveillance	250	300	240*	12	0.4, 0.8
ITCZ volume scan A	125	1200	125	20	0.4, 0.8, 1.2, 2.0, 2.9, 3.7, 4.5, 5.4, 6.3, 7.3, 8.5, 10.0, 11.8, 14.0, 16.8, 20.3, 25, 31.5
ITCZ volume Scan B	125	1200	125	20	0.3, 0.7, 1.5, 2.5, 3.4, 4.1, 5.0, 5.9, 6.8, 7.9, 9.0, 10.0, 11.0, 12.0, 13.1, 15.1, 17.1, 19.2, 21.2, 23.2, 26.3, 29.3, 33.0
Sc volume scan	125	1200	25**	20	3.0, 4.0, 5.0, 6.0, 7.0, 8.0, 9.0, 10.0, 11.0, 12.0, 13.0

*Although technically the maximum possible range at 3000 Hz post repetition frequency is 500 km, the height of the center of the 0.4° elevation scan beam would be 18 km above sea level at this range. A more practical usable range for detection of precipitation echoes is 240 km. At 240-km range, the 0.4° elevation scan beam center is at 5-km altitude and the beam is 6.2 km wide.

**The stratus cloud layer was usually between 1- and 2-km altitude. Transmitter leakage contaminated the first few gates of reflectivity. A 3° elevation beam is at 1.3-km altitude at 25-km range.

NOAA and were incorporated into the National Environmental Satellite, Data and Information Service model initialization.

All of the soundings were made with Vaisala RS80 sondes and sounding data were received, processed, and recorded by Vaisala software running on a DigiCor processor. A mixture of sonde models was used. Forty-five sondes (model 15N.15) used Omega tracking to derive the winds similar to the sondes used at the Integrated Sounding Sites (ISS) in TOGA COARE. The majority of the sondes (204) used Glo-

bal Positioning System (GPS) tracking (model 15G) to derive winds. Vertical resolution of the sonde data was determined by the combination of the data transmission rate and filtering applied to the data before they were stored. Both Omega and GPS systems transmitted thermodynamic data every 1–2 s. These data were median filtered over 11-s intervals. The Omega sonde wind data were transmitted at 10-s intervals and held in a 4-min buffer, from which they were filtered and stored with a final vertical resolution of ~300 m. The GPS sonde wind data were transmitted at 2-s in-

TABLE 7. Distribution of hours during TEPPS cruise associated with several categories of maximum horizontal scale of contiguous radar echo ≥ 20 dBZ (radar-derived convective index).

	$L < 2$ km	$2 \text{ km} \leq L < 10$ km	$10 \text{ km} \leq L < 50$ km	$50 \text{ km} \leq L < 100$ km	$L \geq 100$ km
(a) While on station at 7.8°N, 125°W, 8–23 Aug 1997					
No. of hours	24	23	82	65	184
(b) During eastern Pacific ITCZ leg 28 Jul–25 Aug 1997					
No. of hours	31	39	127	109	369

tervals and were filtered at 60-s intervals to remove the pendulum motion of the sonde package detectable by this more sensitive system. The final vertical resolution of the GPS sonde data was ~30 m. The filtered thermodynamic and wind data were interpolated to 2-s intervals before being written to disk. Omega sonde launches were distributed randomly throughout the cruise except for the 0000 UTC and 1200 UTC launches, which were always GPS sondes. The order of the particular sondes launched was randomized relative to their shipping cases in order to minimize the effect of bases associated with a particular sonde batch.

The procedure for preparing and launching the sonde was designed to minimize heating and cooling of the sonde sensor prior to launch. Sonde temperature, relative humidity, and pressure were compared to reference instruments as part of the sonde preparation procedure. The sondes were released via a launch tube contained in a non-air-conditioned sea container located approximately 10 m above sea level. The 1-min average data at sonde launch time from the surface meteorology time series was used as the first sounding data point. The sonde data were quality controlled at the Joint Office for Science Support (JOSS) at NCAR, using methods similar to those used to quality control the TOGA COARE sounding data (Loehrer et al. 1996, their sections 3a–e).

Overall, we have high confidence in the TEPPS sonde data above 100 m. Only 14 Omega sondes¹ and one GPS sonde exhibited a dry or moist bias.² Below

¹The global Omega tracking system was permanently turned off on 15 September 1997 shortly after completion of the TEPPS cruise. Since the TEPPS cruise was in effect a last chance to use this type of sonde, the Omega sondes obtained for the project came from a variety of sources with a subset having sat on the shelf for years. The Omega sondes used during TOGA COARE in 1992–93 had a dry bias (H. Cole 1997, personal communication). It is therefore not surprising that there was evidence of a difference in the moisture bias between the Omega sonde and GPS sonde batches used during TEPPS.

²The measurement precision of the sonde and Improved Meteorological Measurements from Ships and Buoys (IMET) relative humidity sensor is 4%–5% according to the manufacturer. At the 70%–80% surface relative humidities observed during TEPPS, 2 g kg⁻¹ is the specific humidity equivalent of a 4%–5% relative humidity uncertainty (Y. Serra 1997, personal communication). A sounding was considered to have a high or low moisture bias if the difference between the IMET surface measurement and a mixed layer measurement at 960 hPa derived from the sonde data was outside the range of 1 g kg⁻¹ (predicted by similarity theory) ±2 g kg⁻¹ (i.e., the IMET sensor was subjectively treated as “truth”).

100 m and above the initial surface data point, anomalous temperature and moisture structures were frequently observed in the sonde data. Although these anomalies are generally within the manufacturer-specified instrument error, they appear to be systematic and erroneous. We recommend viewing each sounding before any analysis is undertaken involving the surface layer.

e. Cloud observations

Cloud type and coverage observations following the procedures of the World Meteorological Organization (WMO 1975) were made hourly during daylight hours and on nights with sufficient moonlight to document the visual appearance and nature of clouds in the vicinity of the ship. The visual observations of clouds were documented with digital camera pictures from eight locations around the ship covering nearly 360° of the surrounding area and with conventional film pictures taken from four locations ~90° apart. Selection of the correct classification codes requires observation of the sky as a whole and an almost continuous watch on the sky since certain classifications are related to the evolution and development of individual clouds or to the total cloud cover. Clouds were classified according to the height of their bases into three etages: lower (C_L)—stratocumulus, stratus, cumulus, and cumulonimbus; middle (C_M)—altocumulus, altostratus, and nimbostratus; and high (C_H)—cirrus, cirrocumulus, and cirrostratus. Within each of these etages, nine categories of cloud type are distinguished according to section II.8 of the WMO manual (WMO 1975) with an additional category of 0 indicating no clouds of that type were present. Within the ITCZ, clouds of the low, middle, and high etages were usually present simultaneously, creating a complex cloud field of different types of clouds at different levels. Figure 1 shows the *Brown* on a relatively clear day in the ITCZ. Cirrus clouds are seen above small cumulus in the middle ground with cumulus congestus in the background to the left. Directly behind the ship there is evidence of an anvil associated with a cumulonimbus.

The distribution of cloud cover an okta³ while on station is indicated in Table 9. Large fractions of cloud

³Total cloud cover is the fraction of the celestial dome covered by all clouds visible (WMO 1975). Cloud coverage is reported in terms of oktas (eighths) with 0 corresponding to a completely cloudless sky and 8 corresponding to a completely overcast sky.

TABLE 8. Schedule for upper-air sounding launches during the PACS TEPPS cruise.

Location	Dates	No. of days	Total GPS sondes	Total Omega sondes
Panama to on station	28 Jul–8 Aug	6	32	33
On station	8–23 Aug	6	94	1
ITCZ portion of transit to San Diego	24–25 Aug	12	22	0
Subtropics portion of transit to San Diego	26–29 Aug	2	9	0
Sc region	30 Aug–6 Sep	8	49	11

coverage were more frequent than smaller fractions and the sky was never cloud free while on station. Cumulonimbus (Cb) clouds⁴ were present in 41% of the daytime cloud observations on station in the ITCZ. This percentage should be treated as a lower limit since during rain events at the ship, visibility was reduced and cloud type could often not be identified. The relatively high percentage of Cb cloud occurrence indicates a high frequency of deep convective overturning of the atmosphere in the ITCZ region. The frequency of observed Cb in the eastern tropical Pacific during the TEPPS cruise is higher than that compiled from reports of cooperative observers (~15%) over several decades (Warren et al. 1988). The ENSO conditions may have contributed to the higher than average percentage occurrence of Cb during TEPPS; however, the majority of the difference between the TEPPS and cooperative observer reports is likely a result of the

⁴Low-level cloud classifications $C_L=9$: cumulonimbus with clear fibrous or striated upper part present or $C_L=3$: cumulonimbus without clear fibrous or striated upper part present. The viewable region for visual detection of Cb from the ship was ~100 km in radius. A Cb can be identified when at least the portion above 10 km is visible. Looking up at this angle reduces the path-integrated scatterers and permits detection at further range than surface phenomena. The 100-km distance was derived by comparing photographs of distant Cb with no intervening raining clouds to radar data.

high level of training and motivation of the scientists aboard the *Brown* for the TEPPS cruise (S. Warren 1998, personal communication).

Within the ITCZ, precipitation fell from clouds encompassing a wide range of sizes: from small isolated clouds to large clusters of clouds that formed mesoscale systems (Fig. 6). Small raining cumulus clouds with shallow vertical extent are visible on the left side of Fig. 6a. Figure 6b shows an isolated cumulonimbus (on the horizon on the right side of the photo) within a field of cumulus clouds

under cirrus clouds tinted orange by the setting sun. Two rain shafts from clouds close to the ship that are part of a more extensive contiguous cloud system are shown in the center of Fig. 6c. Within a mesoscale convective system, thick cirrostratus clouds form a canopy over altocumulus clouds with virga (right of center) and a line of cumulus clouds at low levels in Fig. 6d.

Visual observations of near-surface phenomena such as rainshafts are usually possible up to 50-km range if the intervening air is exceptionally clear (McCartney 1976; Barrett and Grant 1979). Rainfall was visually observed during the day roughly half the time while on station. Forty-five percent of the hours documented by cloud photographs contained clear evidence of rainfall in the vicinity of the ship. A similar percentage contained clear evidence of no rainfall in the vicinity and roughly 10% were indeterminate.

f. *Surface time series*

Surface meteorological and upper ocean data were obtained at 10-s intervals. The atmospheric instrumen-

TABLE 9. Distribution of cloud cover in okta (eighths) for hours it was observable during time on station in the ITCZ. Cloud cover was observable during daylight hours and at night when sufficient moonlight was present.

	Cloud coverage in okta							
	1	2	3	4	5	6	7	8
No. of hours	10	22	32	29	27	51	82	86

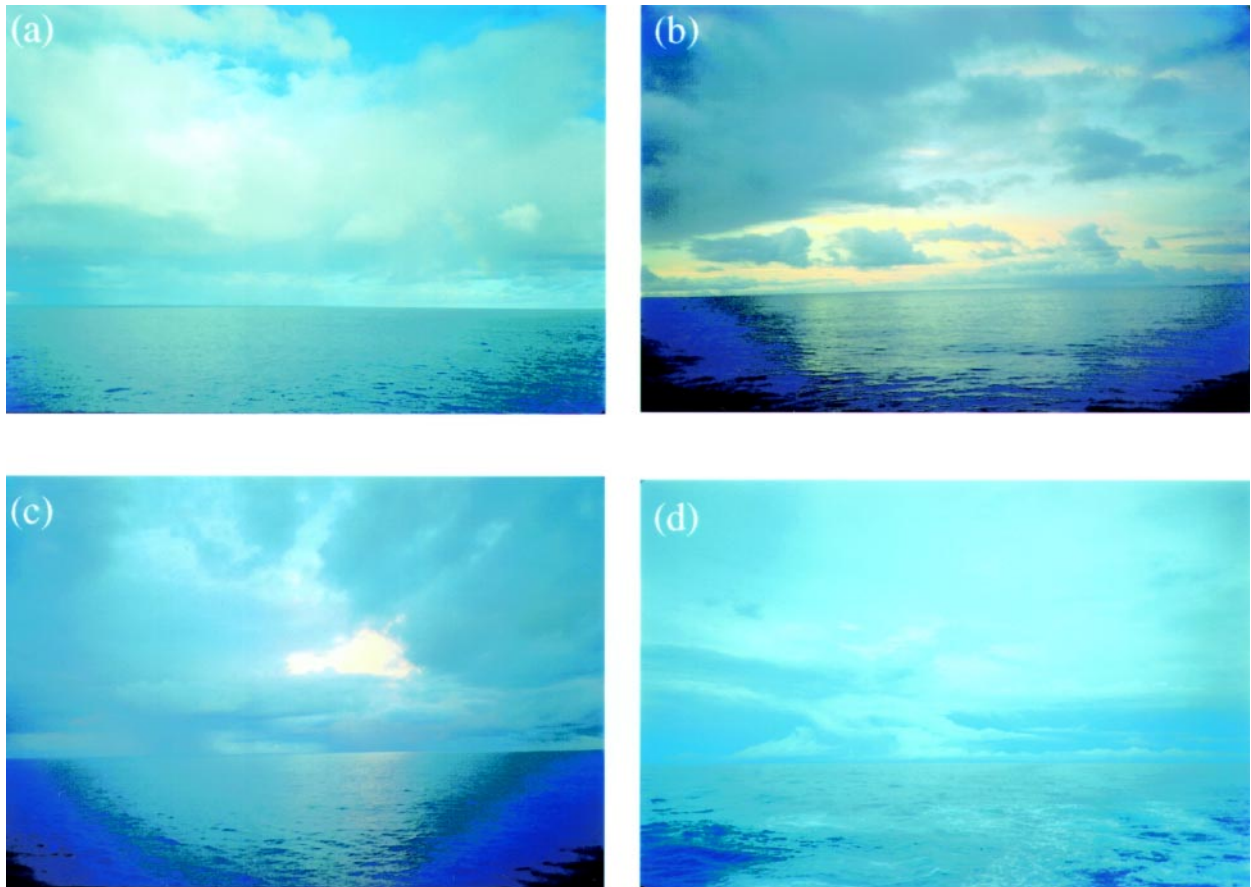


FIG. 6. Photographs of different scales of precipitating clouds seen while on station in the eastern Pacific ITCZ. (a) Isolated, small, shallow cumulonimbus in left background; note rainbow in right foreground indicating that the foreground cloud is lightly precipitating, (b) isolated cumulonimbus of moderate vertical extent surrounded by cumulus clouds with cirrus at upper levels, (c) scattered cumulonimbus of moderate vertical extent, and (d) cumulonimbus underneath cirrus anvil within a mesoscale convective system at 0000 UTC 24 Aug 1997. Virga is visible falling from midlevel cloud on left.

tation used was similar to that deployed on operational buoys in the TAO array (Hayes et al. 1991) and the PACS research buoys deployed by the Woods Hole Oceanographic Institute and the University of South Florida (Fig. 4). Descriptions of the surface meteorological and upper ocean instrumentation onboard the *Brown* for the TEPPS cruise are provided in Table 10. The wind speed and direction, temperature, and relative humidity sensors and one of the siphon gauges are part of an integrated system called ASIMET (Air Sea Interaction Meteorology) provided by Principal Investigator R. Weller of the Upper Ocean Processes Group at the Woods Hole Oceanographic Institute (Hosom et al. 1995). Most of the ASIMET sensors were mounted on a boom at the bow of the ship so that disturbance of the atmospheric characteristics by the ship itself would be minimized. Instruments that did not require undisturbed air—the radiometer and pressure sensor—were mounted at suitable locations on the 03

and 04 levels (Fig. 3). Information on the calibration and accuracy of these sensors is provided in appendix A.

The seawater intakes for the sea surface temperature, conductivity, and CO₂ fluorometer (Wanninkhof et al. 1998) measurements were near the bow of the ship on the starboard side in the vicinity of the bow thrusters. The depth of the intake was switched from 4.88 m when the ship was under way to 2.13 m when the ship was on station (while under way the shallower intake is not always underwater and flow to the instruments can be disrupted). Use of the bow thrusters for station-keeping mixed the upper layer of seawater in the vicinity of the ship. Our upper-ocean measurements are thus more representative of average conditions over the first few meters of depth than at the specific depth of the intake.

The small-scale variability of surface meteorological variables observed within precipitating events is

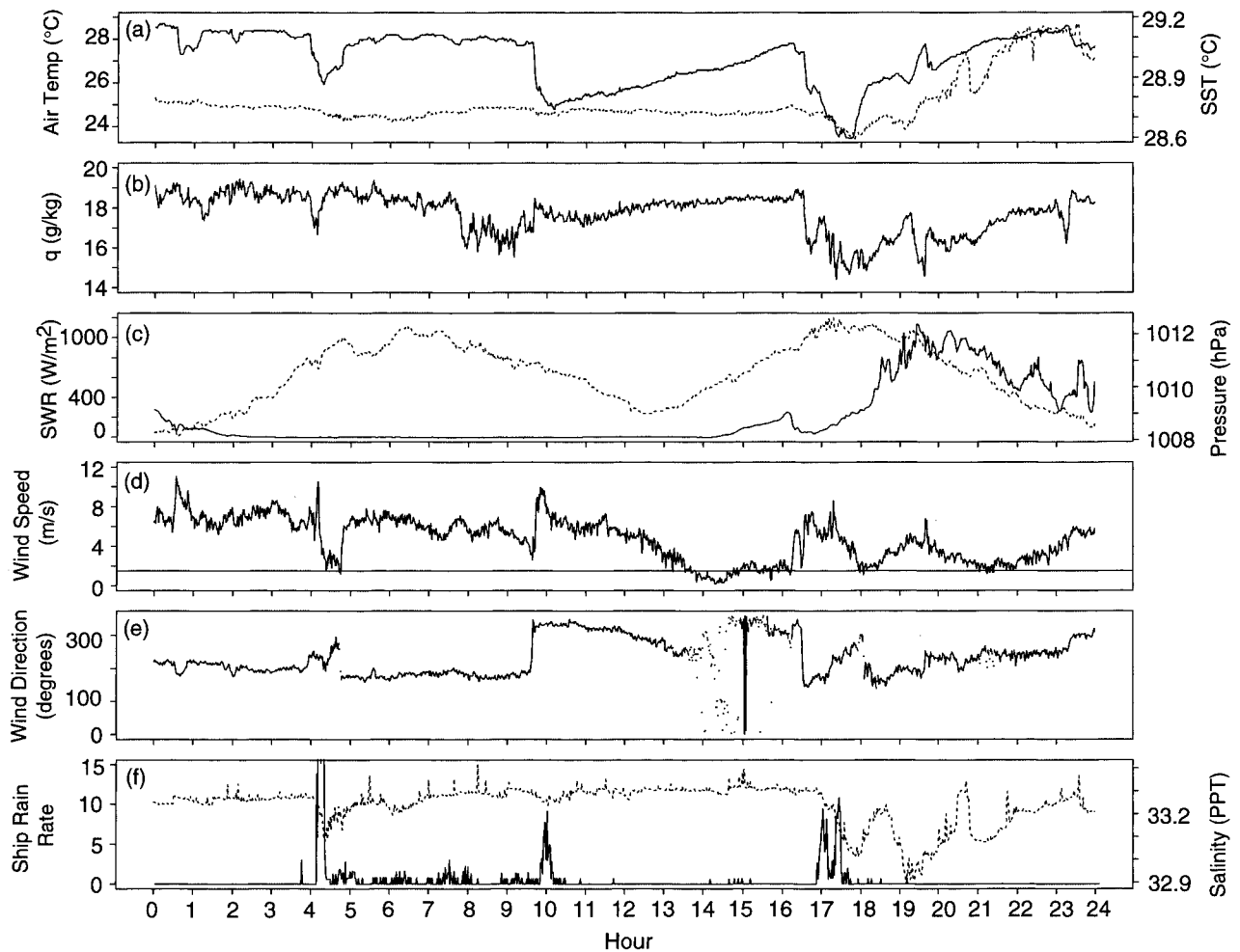


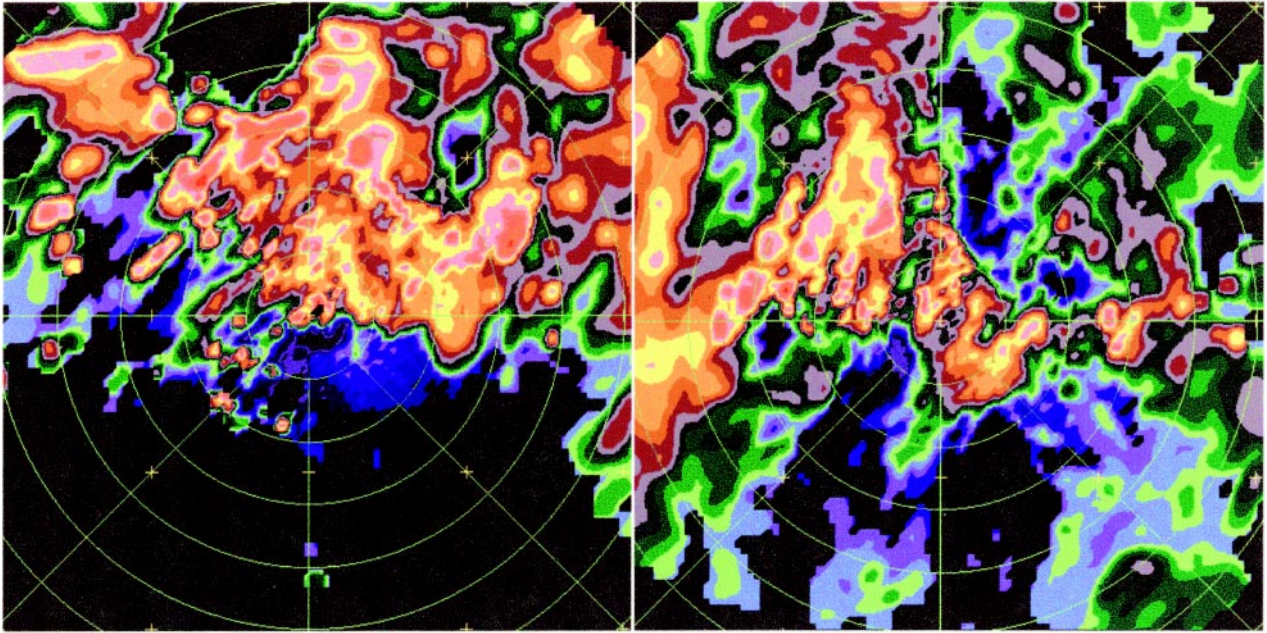
FIG. 7. One-minute average time series of surface meteorological and upper-ocean data from the *Brown* on 11 Aug 1997. (a) Air temperature (solid line) and SST (dashed line), (b) specific humidity, (c) shortwave radiation (solid line) and sea level pressure (dashed line), (d) wind speed, (e) wind direction (from which the wind blows), and (f) rain rate from IM ship rain gauge (solid line) and salinity (dashed line). When wind speeds are below 1.5 m s^{-1} [horizontal line in (d)], the wind direction data are unreliable and are indicated by dots in (e). (IM ship rain gauge data courtesy of M. Grossklaus.)

illustrated by the time series data obtained on 11 August 1997 while on station (Fig. 7). Sunset was at 0230 UTC (1930 LT) and sunrise was at 1430 UTC (0730 LT) (Fig. 7c). Data in Fig. 7 are averaged over 1 min and are presented unfiltered (i.e., without removal of diurnal or semidiurnal cycles). Since the exact relationship among the rainfall measurements on ship and the amount of water reaching the ocean surface is under study, for the purposes of this discussion, the IM ship rain gauge is used as an indicator of rainfall presence and its relative intensity. The TEPPS air temperature and specific humidity values (Fig. 7) were generally lower than those in the western Pacific warm pool during TOGA COARE (Weller and Anderson 1996) since the sea surface temperatures are lower in the eastern Pacific.

The two primary rain events on 11 August 1997 were from 0400 to 1030 UTC during the night and from 1650 to 1830 during the day. The impact of freshwater flux on the upper ocean is strongly related to the diurnal cycle (incoming shortwave radiation) and wind forcing (Anderson et al. 1996). The mixed layer shoals when wind stress is weaker. During the night, the upper-ocean mixed layer is convectively unstable and freshwater at the surface can more readily mix downward, while during the day, the stability of the mixed layer inhibits freshwater mixing. Wind speeds immediately after the heavy rain periods at 0415 UTC and 1700 UTC were $< 4 \text{ m s}^{-1}$. The inhibited mixing of freshwater during the day is clearly evident in the salinity time series where the heavy rains (maximum of 44 mm h^{-1}) at 0415 UTC (Figs. 7f, 8a)

(a) 0416

(b) 0937



(c) 1701

(d) 1901

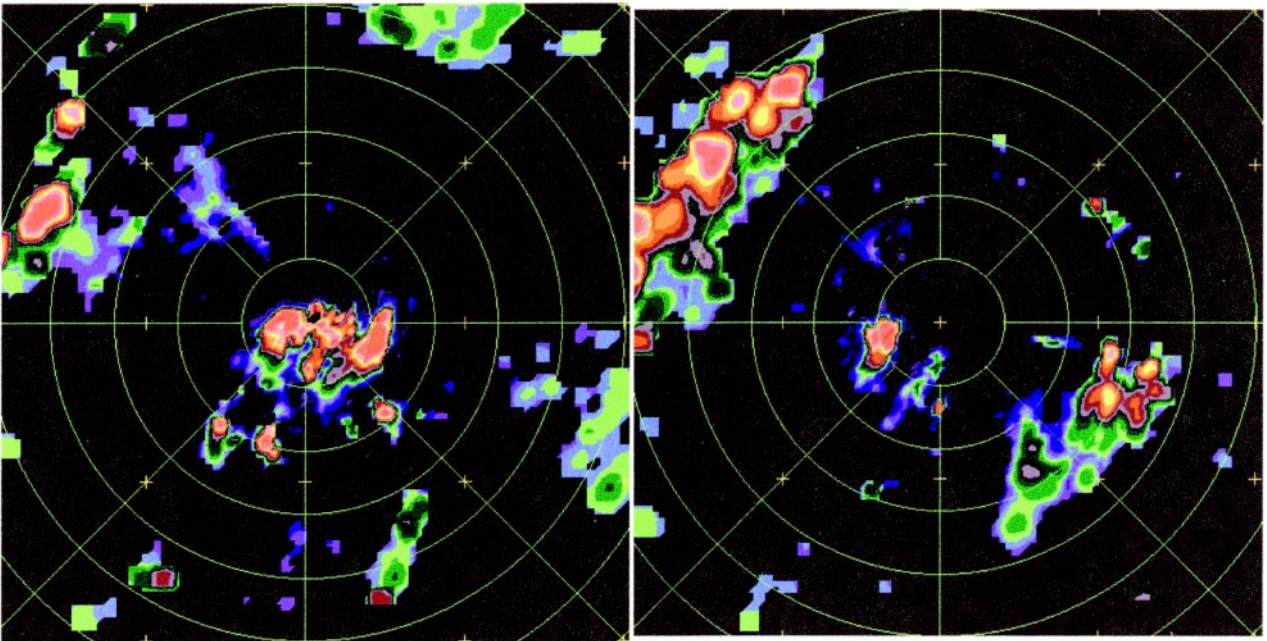


FIG. 8. Low-level reflectivities (0.5-km altitude) from shipboard C-band radar on 11 Aug 1997. Time in UTC. Image is centered on position of ship on station. Range rings are at 20-km intervals.

yielded only a 0.2 ppt drop in salinity while the lower rain rates (maximum of 10 mm h^{-1}) at 1700 UTC (Figs. 7f, 8c) were associated with a 0.3 ppt drop in salinity. The most dramatic drop in salinity during the 24-h period occurred at 1900 UTC and was not associated with rainfall at the ship itself (Fig. 7f). The radar data show the nearest precipitation to be about 20 km in dimension and 20 km to the southwest (Fig. 8d). It is likely that the low salinities measured by the ship at 1900 UTC were the result of freshwater advected to the location of the ship from a heavier raining portion of the precipitation region that intersected the ship at 1700–1730 UTC.

Over the 24-h period, the largest changes in air temperature and specific humidity were associated with the small shower at 1700 UTC rather than the convective cells of the large precipitating region at 0415 UTC (Figs. 7a,b and 8a,c). Wind speed underwent the most dramatic changes of the day at 0415 UTC, dropping from 10 to near 2 m s^{-1} within the heavier rainfall near the forward-moving edge of a large precipitation region. In contrast, wind speed increased during the $5\text{--}10 \text{ mm h}^{-1}$ rainfall period at 1000 UTC and decreased slowly during the rain event at 1700 UTC.

At 0940 UTC near the back of a lightly precipitating region (rain rates $< 2 \text{ mm h}^{-1}$) several abrupt changes in the observed meteorological conditions occurred (Figs. 7, 8b). The temperature dropped nearly 3°C in 10 min and continued to decrease until 1010 UTC. The wind speed first dropped slightly then increased by 5 m s^{-1} within 10 min and the wind direction shifted from 190° to 340° . These changes in combination indicate a change in the air mass over the ship 20 min prior to the onset of stronger rain rates of up to 9 mm h^{-1} at 1000 UTC.

From the above example, it is evident that the scanning C-band radar on the *Brown* can place the shipboard meteorological time series into a broader meteorological context with shorter time and spatial scale data than available from satellite data. Radar reflectivity data can provide a detailed picture of the size and duration of precipitating clouds in the vicinity and Doppler velocity data provides information on the three-dimensional airflows within precipitating

clouds. Without this context provided by radar, the time variations at the ocean surface would be difficult to interpret *unambiguously*. Supplemental information from the ship-based profilers and cloud photography also aids in characterizing the context of the surface measurements. In this way, ambiguities in the physical interpretation of the surface time series data can be resolved and methods for distinguishing and removing data influenced by local convection versus data that is more representative of large-scale conditions can be tested and refined for eventual application to surface data from buoys in the region.

g. Profilers

The primary purposes of the 915-MHz profiler and RASS in TEPPS were to measure the vertical profiles of horizontal winds and virtual temperature. The 915-MHz profiler also obtained vertical profiles of reflectivity, Doppler velocity, and spectral width. The profilers were mounted on the stern on the main deck as low to the water as possible to minimize the effects of sea clutter seen in other ship installations (Hartten 1998). The 915-MHz profiler antenna was stabilized mechanically to compensate for the roll and pitch of the ship. The S-band profiler provided profiles of radar reflectivity, Doppler velocity, and spectral width along the beam at 1-min intervals. The S-band profiler was not stabilized and pointed nor-

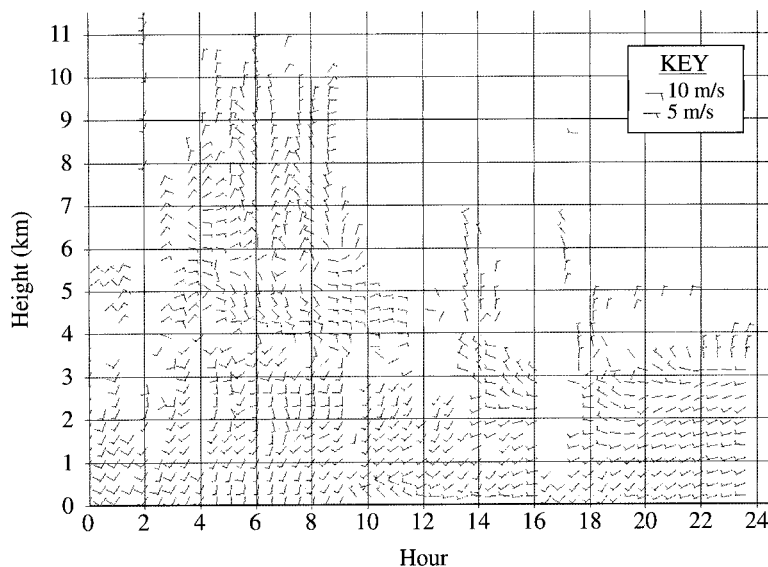


FIG. 9. Time–height plot of 30-min consensus horizontal winds from the 915-MHz profiler on 11 Aug 1997. Time associated with the column of winds is start time of averaging interval. For example, wind barbs at 1200 UTC are averages for data obtained from 1205 to 1230 UTC. (Data courtesy of C. Williams, CIRES.)

TABLE 10. Summary of surface meteorological and oceanographic sensors on the *Brown* during the PACS TEPPS cruise.

Sensor	Type	Location	Height above water line (m)
Wind speed and direction	WHOI-modified R. M. Young prop/vane Model 05103	Mast on bow	14.12
Air temperature and relative humidity	WHOI-modified Rototronic MP-101A with R. M. Young multiplate radiation shield	Mast on bow	12.98
Shortwave radiation	WHOI-modified Eppley Precision Spectral Pyranometer	On pole mounted on center forward 02 level	10.7
Barometric pressure	Atmospheric Instrumentation Research Inc. Model DB-2A with Gill static pressure port	Port 04 level	15.56
Wave height	TSKA, Inc., remote wave meter	On bow	7.62
Rain rate	Scientific Technology Inc. Optical rain gauge Model ORG-115-DA	Port forward 03 level Top of winch house	12.57 13.05
	IfM ship rain gauge	Center forward 03 level	12.17
	Joss-Waldvogel distrometer	Top of van on inside port 02 level van space	11.84
Raindrop distribution	Pizeoelectric distrometer (2)	Top of van on inside port 02 level van space	11.79
	IfM ship distrometer	Port 03 level	12.95

mal to the main deck of the ship. Of these variables, radar reflectivity is the only one not sensitive to contamination by horizontal winds when the beam is not pointed precisely vertically. The shorter wavelength of the S-band profiler contributes to its greater sensitivity compared to the 915-MHz profiler. The S-band profiler can measure weaker radar echoes and map the structure of the storm within ice regions to a higher altitude.

The profilers were supplied and operated by Principal Investigator K. Gage of the NOAA Aeronomy

Laboratory. The specifications of the 915-MHz (Carter et al. 1992; Gage et al. 1994; Carter et al. 1995) and S-band profilers (Ecklund et al. 1995) are provided in Table 11. In the ITCZ, both profilers were operated alternately in 495-m (up to 18.9-km altitude) and 105-m (up to 6.7-km altitude) pulse length modes during each 25-min sampling period. A detailed description of the profiler sampling during each half hour is provided in appendix B.

The vertical profiles of the 25-min average winds on 11 August 1997 (Fig. 9) shows the layer of south-

TABLE 10. *Continued.*

Sensor	Type	Location	Height above water line (m)
Rain temperature (wet-bulb temperature during rain events)	WHOI custom design	05 level	17.73
	WHOI-modified R. M. Young self-siphoning rain gauge Model 50201	Mast on bow	13.99
Rain accumulation		02 level stbd	10.31
	R. M. Young self- siphoning rain gauge Model 50202 (7)	02 level port	10.31
		03 level stbd	12.83
		03 level port	12.83
		05 level stbd	17.73
		05 level port	17.73
		Top of winch house	13.31
Ocean surface temperature and conductivity	Sea-Bird Electronics 21 Seachest Thermosalinograph	20 m from bow along stbd side (on station) (under way)	-2.13 m -4.33 m
CO ₂ fluorometer	Wanninkhof et al. (1998)	Same intake as thermosalinograph	

erly winds within the precipitating region to be 3 km deep from 0400 UTC to 0900 UTC. The abrupt changes in the time series data and the change in air mass at 0940 UTC (Fig. 7) were associated with a shallow layer (~500 m deep) of northwesterly winds (Fig. 9), which persisted for ~2 h. By 1400 UTC, winds from the surface to 3-km altitude had shifted to westerly and remained westerly to southwesterly until the end of the day. While the 3-km deep layer of southerly winds earlier in the day was associated with organized convection with the scale of 20-dBZ contiguous echo > 100 km (Figs. 8a,b), the 3-km deep layer of westerly winds later in the day was associated with a period of smaller-scale precipitating systems (Figs. 8c,d).

Decreases in reflectivity with decreasing height in the high-resolution vertical pointing S-band radar data from 11 August 1997 indicated that evaporation often reduced precipitation formed aloft on its way to the surface (Fig. 10a). Evaporation was particularly evident at ~1430 UTC where reflectivities up to 25–30 dBZ at 1-km altitude decreased to ~10 dBZ just

above the surface and registered only a trace of precipitation at the IM rain gauge (Fig. 7f).

The high-resolution vertical profiles of reflectivity from profilers (e.g., Fig. 10) can be used to distinguish between convective and stratiform precipitation processes (Williams et al. 1995; Gage et al. 1996). A radar brightband of varying thickness associated with stratiform precipitation was intermittently present from 0300 to 1000 UTC. The high-resolution documents finescale fall streaks within the stratiform region. The shorter duration precipitation event at 1700 UTC was associated with reflectivities > 40 dBZ over the ship from the surface to 4.5-km altitude, a reflectivity pattern associated with convective precipitation processes. From 1830 to 1900 UTC, the profiler showed no precipitation echo over the ship, confirming that the low salinities at 1900 UTC (Fig. 7f) were associated with rainfall in the vicinity rather than over the ship itself. The detailed vertical structure of these data will aid in linking the lower-resolution scanning radar data to satellite data.

TABLE 11. Basic characteristics of NOAA Aeronomy Laboratory profilers used on the TEPPS cruise.

Parameter	915 MHz	S band (2835 MHz)
Wavelength	33 cm	10.6 cm
Peak power	500 W	380 W
Antenna	2-m phased array	3-m shrouded dish
Beamwidth	9°	3°
Pulse length	60, 105, and 495 m	60, 105, and 495 m
Number of points in Doppler spectra	256	256
Nyquist velocity	17.7 m s ⁻¹	17.7 m s ⁻¹
Doppler velocity resolution	13.8 cm s ⁻¹	13.8 cm s ⁻¹
Dwell time	30 s	30 s
Stabilization	Mechanical	None

4. Temporal variation of precipitation in the eastern Pacific ITCZ

a. Eastern Pacific ITCZ environment

The 4-hourly upper-air sounding data obtained during the time on station at 7.8°N, 125°W are shown in the time–height plots of zonal wind, meridional wind, and relative humidity in Fig. 11. The plots show the observed data from each upper-air sounding and are not smoothed. White areas within the plot indicate missing data from sondes that terminated prior to reaching 100 hPa.

Zonal winds alternated between easterly and westerly near the surface and were usually weak (less than 5 m s⁻¹ in magnitude). At 200 hPa, zonal winds were almost exclusively easterly with magnitudes up to -20 m s⁻¹ (Fig. 11a). During the time on station, there were three periods of sustained surface southerlies > 2 m s⁻¹ on 10–11, 14–15, and 19 August (Fig. 11b). Two out of the three surface southerly events were accompanied by deep northerly winds aloft. Northerly winds extended from 575 to 125 hPa on 10–11 August and to slightly lower levels on 19 August. The 14–15 August surface southerlies were not accompanied by deep northerly winds aloft. The magnitudes of the

surface southerly wind and the vertical shear were strongest on 10–11 August when the meridional wind reached 10 m s⁻¹ near the surface, up to -13 m s⁻¹ at 500–350 hPa, and peaked at -18 m s⁻¹ between 150 and 125 hPa. These magnitudes were less than the strongest zonal shears observed in TOGA COARE during the period of strong surface westerlies in late December 1992 where the 5-day running mean 800-hPa zonal winds were 15 m s⁻¹ and 150-hPa zonal winds were -20 m s⁻¹ (Lin and Johnson 1996). Similar to the western Pacific ITCZ (Reed and Recker 1971) and the eastern Atlantic ITCZ (Burpee 1975; Burpee and Reed 1982), the largest variation in the surface winds and the strongest vertical shears in the eastern Pacific ITCZ were in the meridional component of the wind.

The levels with the largest humidity fluctuations in the eastern Pacific ITCZ were between 500 and 300 hPa, somewhat higher than corresponding levels in the western Pacific ITCZ, which are near 600 hPa (Reed and Recker 1971). The relative humidity data were marked by three periods of extreme dryness above 400 hPa on 9–10, 13–14, and 17–18 August and to a lesser degree on 23 August (Fig. 11c). The drying at midlevels precedes and in some cases overlaps with the beginning of the periods of sustained surface southerlies. Moist air above 500 hPa is associated with the latter portion of the sustained surface southerly events and lasts for about 24 h after they have ended. As will be shown in the next section, the sustained surface southerly events were associated with periods of more organized mesoscale convective activity; thus, it is likely that the moister air above 500 hPa was a result of mesoscale convective activity.

b. Radar-observed convection

The time series of the hourly radar-derived convective activity index (section 3b) is shown for the period on station in the ITCZ in Fig. 11d. These data have been averaged into daily values and plotted in Fig. 12a for comparison to convective indices derived from the IR and microwave data.

The degree of mesoscale organization (Fig. 11d) often varied from hour to hour and did not always make a smooth transition between adjacent categories (i.e.,

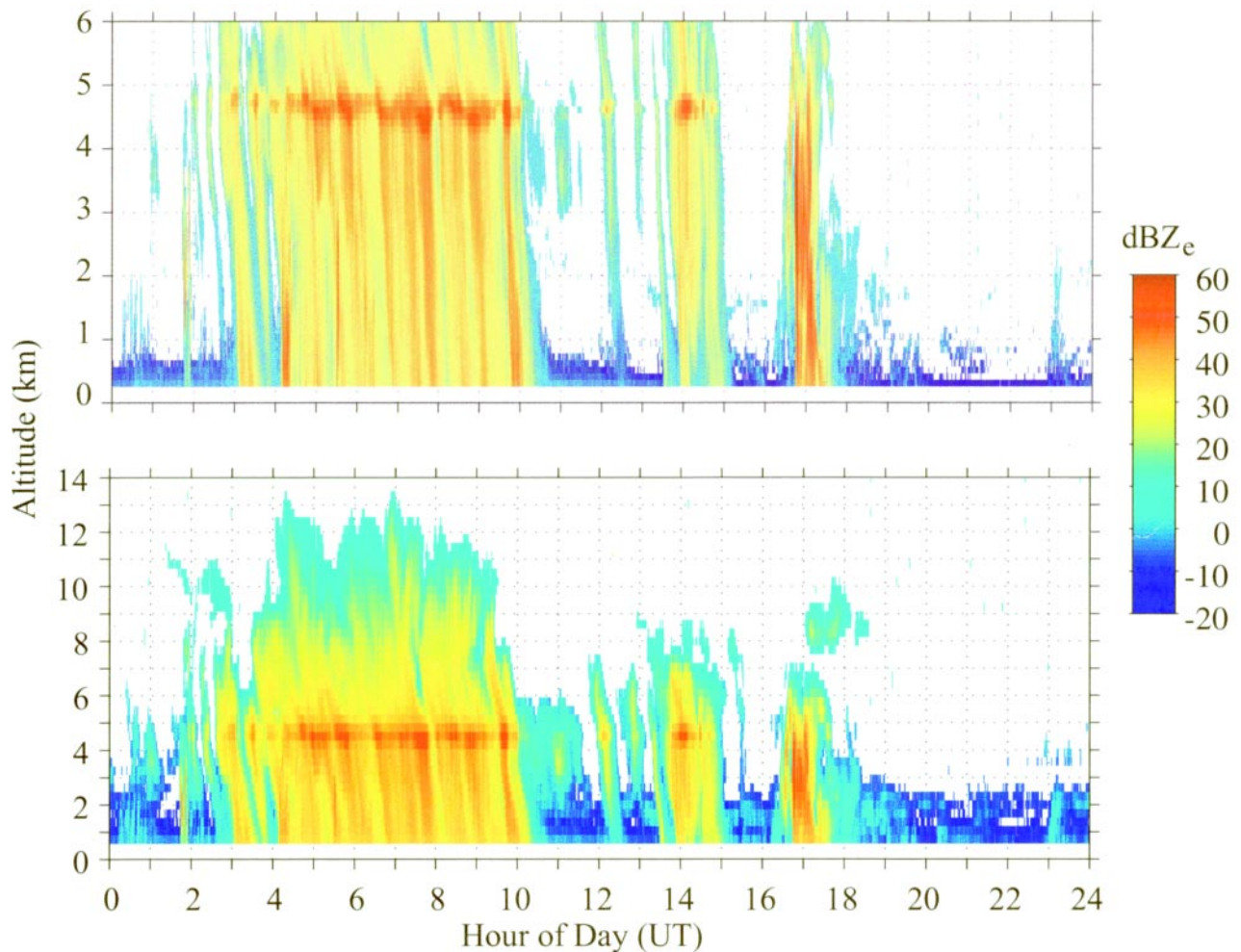
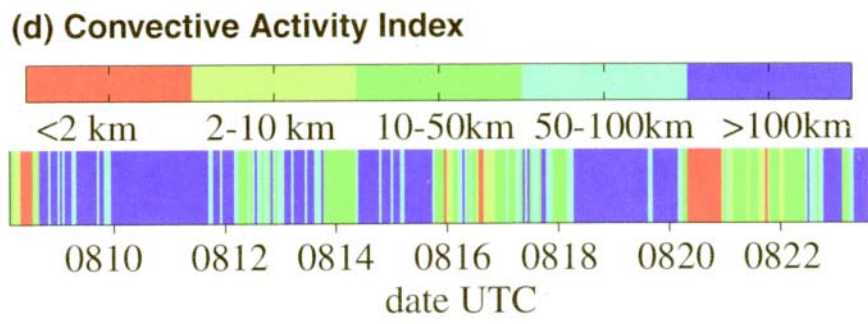
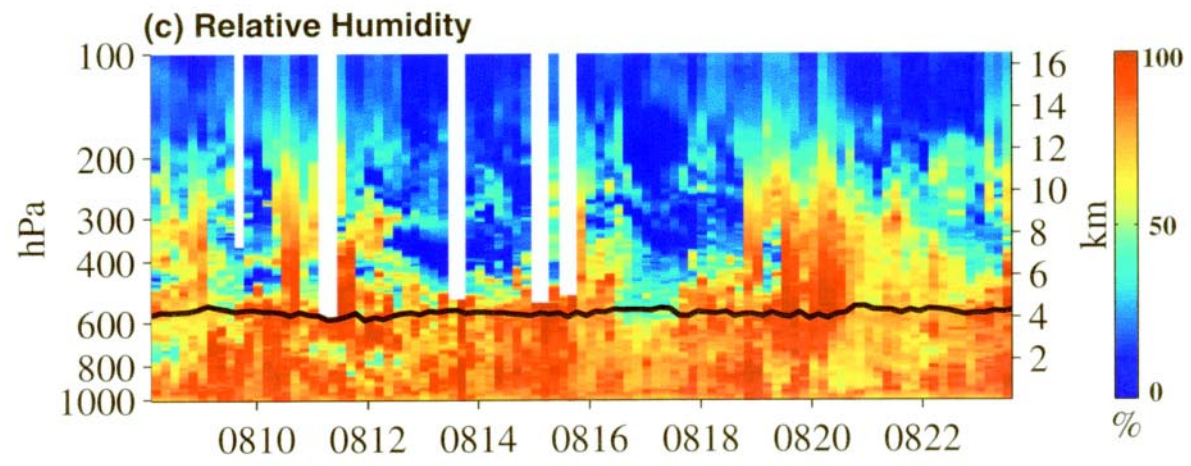
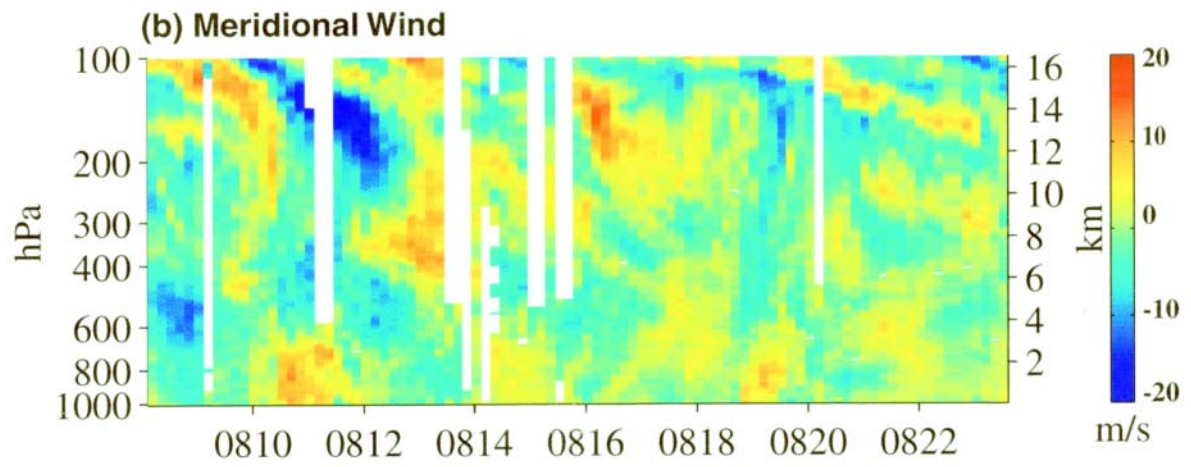
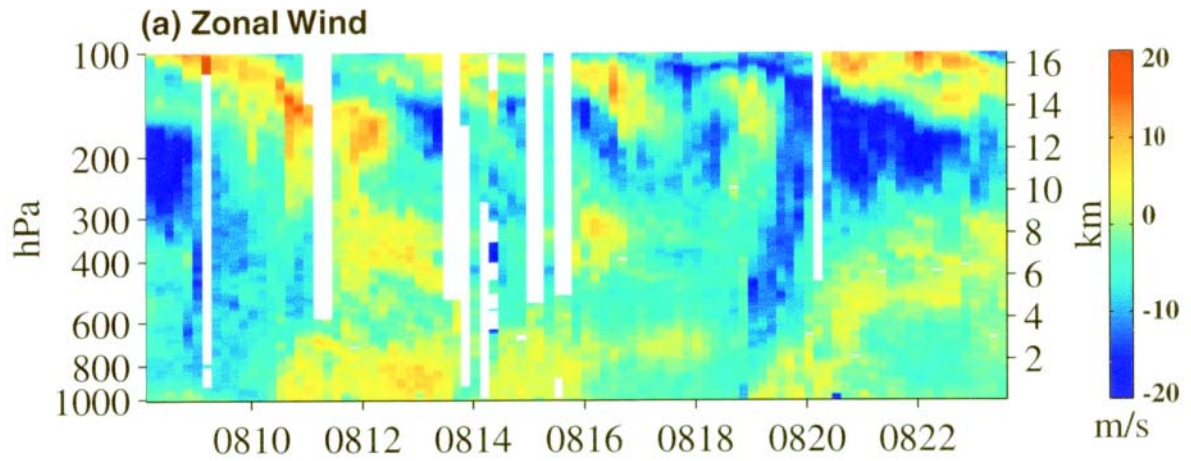


FIG. 10. Vertically pointing S-band radar reflectivities from 2835-MHz profiler on 11 Aug 1997: (top) 100-m pulse mode and (bottom) 500-m pulse mode. (Figure courtesy of C. Williams, CIRES.)

16 August, 23 August). While on station, longer sustained periods (> 24 h) of a high degree of mesoscale organization ($L > 50$ km) occurred between 2300 UTC 9 August and 6000 UTC 12 August, between 1100 UTC 14 August and 1800 UTC 15 August, and between 0700 UTC 18 August and 0300 UTC 20 August. These three periods of sustained high degrees of mesoscale organization are associated with periods of stronger surface southerly winds (Fig. 11a). The 19–20 August 1997 time period corresponding to the longest sustained period of convective activity larger than 100 km in scale was also associated with the deepest layer of moist air with relative humidities up to 90% reaching 300 hPa (Fig. 11c).

Over seasonal timescales, the thermally direct circulation between the equatorial cold tongue and warmer waters several degrees to the north yields southwesterly winds over the region of the TEPPS on-

station observations (Mitchell and Wallace 1992). The association of periods of enhanced mesoscale convective activity within the ITCZ with stronger southerly winds (Fig. 11) imply a larger-scale *atmospheric* regulation of the local degree of mesoscale organization with a timescale of days. The regulation is more likely dominated by the atmosphere than the ocean since these timescales are too short to be associated with changes in SST over broad regions. These results suggest that the shorter timescale perturbations on the mean seasonal atmospheric conditions may be more directly associated with the formation of mesoscale convective systems in the ITCZ than the mean conditions themselves—an indirect indication that atmospheric waves may be regulating the degree of convective organization. The timescale of inertial instability associated with southerly winds and off-equatorial organized convection as discussed by Tomas



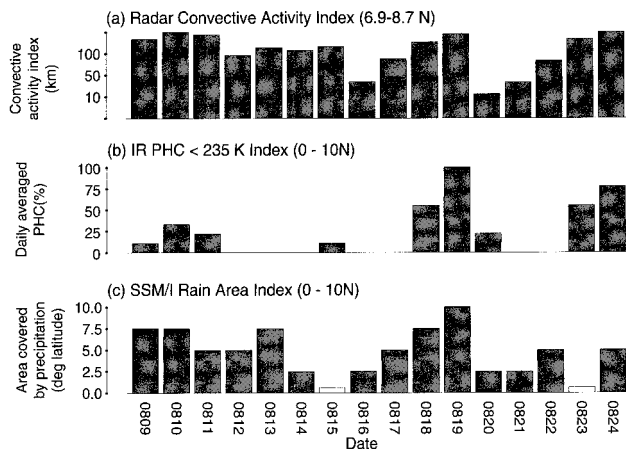


FIG. 12. Histograms of daily radar and satellite indices of horizontal scale of precipitation activity in vicinity of the ship. (a) Daily average radar convective activity index from shipboard radar (section 3b); (b) index from 0 to 4 of frequency of pixels with IR brightness temperature < 235 K between 0°–10°N at 125°W, and (c) size of cumulative daily precipitation area between 0° and 10°N at 125°W latitude from Ferriday SSM/I precipitation estimation algorithm. Hollow bars indicate missing data.

and Webster (1997) is consistent with the timescale of larger, persistent precipitation regions observed by radar during TEPPS. Further study is needed to determine if there is a relationship between the wave structure and mesoscale convective systems as seen in the western Pacific ITCZ (Reed and Recker 1971) or the eastern Atlantic ITCZ (Burpee 1975; Burpee and Reed 1982).

c. IR high cloudiness

A frequently used measure of convective activity is percent high cloudiness (PHC) from infrared satellite data (e.g., Chen et al. 1996). A time–longitude plot of average daily cold cloud < 235 K for the eastern Pacific ITCZ region during August 1997 is shown in Fig. 13. The location of the ship is indicated by the vertical line at 125°W. The plot generally does not contain clearly propagating features, but the time series may be too short to identify propagation. Nonetheless, alternating regimes are evident. Between 180° and 135°W, PHC exhibits a ~5–6 day cycle.

FIG. 11. Time–height plots of (a) zonal wind, (b) meridional wind, and (c) relative humidity from four hourly GPS sondes launched while on station at 7.8°N, 125°W. Vertical resolution of the data is 30 m. (d) Hourly radar convective activity index (see section 3b) while on station. (Figure courtesy of Y. Serra, University of Washington.)

Along 125°W, high cloudiness < 235 K is present to a lesser degree in the daily averages on 9–11 August, and to greater degrees on 18–19 August and 23–28 August. Periods where high cloudiness is absent are 1–3, 6–8, 12–17, and 20–22 August. To facilitate comparison with radar- and microwave-derived convective indices, the daily frequency of IR temperature < 235 K within the ~2° long band centered on 125°W from 0° to 10°N has been coded into an index from 0% to 100% and displayed as a bar plot in Fig. 12b.

d. Microwave-derived precipitation area

The areal coverage of Special Sensor Microwave/Imager (SSM/I)-derived precipitation was also coded into an index derived from daily precipitation maps produced by the method of Ferriday and Avery (1994). This algorithm uses both the absorption and emission channels of the SSM/I to derive rain rate from microwave brightness temperatures using an empirical solution derived from cloud model and radiative transfer calculations. Although different microwave algorithms produce different estimates of precipitation, several formal algorithm intercomparison projects have shown that the differences among the various microwave algorithms are smaller than the differences between microwave algorithms and algorithms based on IR data (Ebert et al. 1996). The precipitation estimates of the Ferriday–Avery algorithm were near the center of the distribution of estimates for the 20 SSM/I microwave algorithms examined in the WetNet Precipitation Incomparision Project (Smith et al. 1998). For the purposes of this paper, Ferriday–Avery algorithm SSM/I precipitation estimates will be used as a representative of microwave algorithm precipitation estimates versus IR-derived precipitation estimates.

To construct the convective index for microwave-derived precipitation, the ~2° wide longitude band centered at 125°W from 0° to 10°N was examined in the daily SSM/I-derived precipitation maps. The fraction of net area covered by precipitation in the daily SSM/I maps within this band was rounded to the nearest 25% (area equivalent of 2.5° in latitude) to obtain a crude index of daily SSM/I precipitation area (Fig. 12c).

e. Validation of satellite-derived precipitation occurrence

Comparison of the various indicators of daily convective activity—the average scale of largest contiguous radar echo, the area of IR cold cloudiness, and the SSM/I raining area (Fig. 12)—aids in evaluating

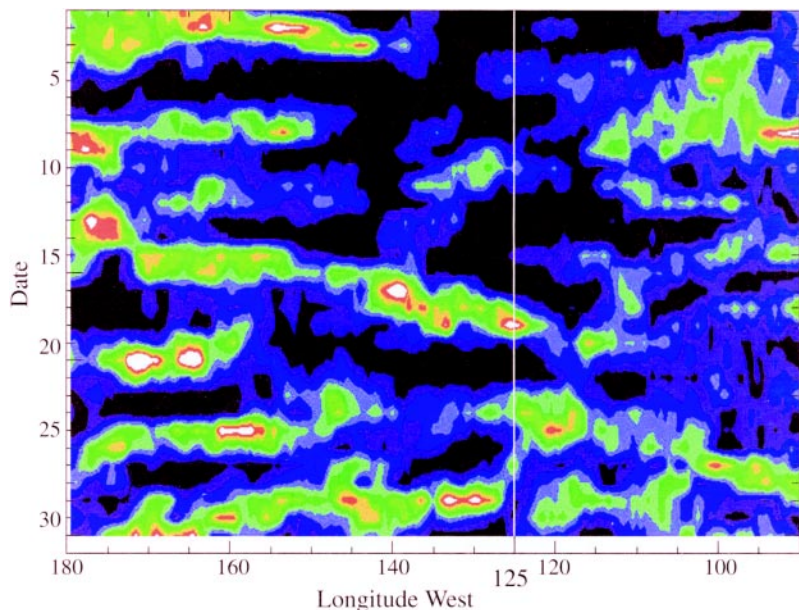


FIG. 13. Time–longitude plot of Aug 1997 daily average cold cloud ($T < 235$ K) for equator 0° – 10° N. Frequency of high cloudiness is color coded in increments of 10%. At the two ends of the scale, black indicates 0%–10% of IR pixels < 235 K and white indicates 90%–100% of IR pixels < 235 K. Line indicates ship location. (Figure courtesy of B. Mapes, CIRES.)

the efficacy of satellite-derived methods for characterizing the temporal distribution of convective activity in the tropical eastern Pacific. Although the radar-derived index covers only the area from $\sim 6.9^{\circ}$ to 8.7° N, it most directly indicates the scale of mesoscale organization supportable by the atmosphere and is useful in validating the satellite indices. The three convective periods on station with the longest sustained periods of high mesoscale organization (rounded to the nearest day) are 10–11, 14–15, and 18–20 August. These three time periods have some expression in all three convective activity indices. Therefore, *when a convective event is large in scale and long in duration, any of the satellite-precipitation methodologies will detect the associated rainfall.*

However, on three occasions when the satellite IR index showed no cloudiness < 235 K (12–14, 16–17, and 21–22 August), both the SSM/I rainfall areas and radar-derived convective activity indices were not zero. The convective systems missed by the IR cold cloudiness index were not exclusively small, isolated convective cells but included echoes > 100 km in scale whose satellite-detected cloud tops were warmer than 235 K. SSM/I-derived rainfall for 12–14 August covered an area of 2.5° – 5° and the radar-derived convective indices indicated radar echoes with maximum dimension > 100 km for 1–9-h duration (Figs. 11d, 12c).

On 17 August, a raining area approximately 5° in scale was present according to SSM/I data, and radar echoes had maximum dimension > 100 km for 1–2-h duration (Figs. 11d, 12c). If these systems had had cloud tops < 235 K they would have been of sufficient size to be resolved by the IR cold cloudiness measure.

The trend of SSM/I rain area exhibited generally fair agreement with the radar convective activity (Fig. 12). In contrast, cold cloudiness < 235 K was associated with only a *subset* of the precipitating systems in the eastern tropical Pacific. The large systems (> 100 km) with long duration (> 24 h) tended to contain some cloudiness < 235 K, while the convective systems of shorter duration (< 24 h) sometimes exhibited no cold cloudiness < 235 K. The comparison of ship radar, IR cold cloudiness, and microwave indices thus indicates that in the

eastern Pacific ITCZ microwave methods have greater skill in detecting the existence of precipitation within a large area than do IR methods.

Figures 11d and 12 indicate that during periods when high cloudiness < 235 K was absent in the eastern tropical Pacific, convection was active and producing rainfall over areas at times greater than 50 km and infrequently > 100 km in contiguous echo dimension. What appears to be suppressed during these periods is not convection per se, but rather the *organization* of convection into sustained, large (> 100 km in dimension) mesoscale convective systems.

5. Spatial variation of precipitation—Comparisons of instantaneous radar echo and microwave-derived precipitation

Different three-dimensional storm structures can produce the same areal average surface rainfall, so the mapping of storm structure to rainfall amount is not unique. It is therefore not surprising that previous studies have shown that the correlation of instantaneous IR data and reflectivity data tends to be weak (Heymsfield and Fulton 1988; Adler et al. 1983; Yuter and Houze 1998). The GOES Precipitation Index

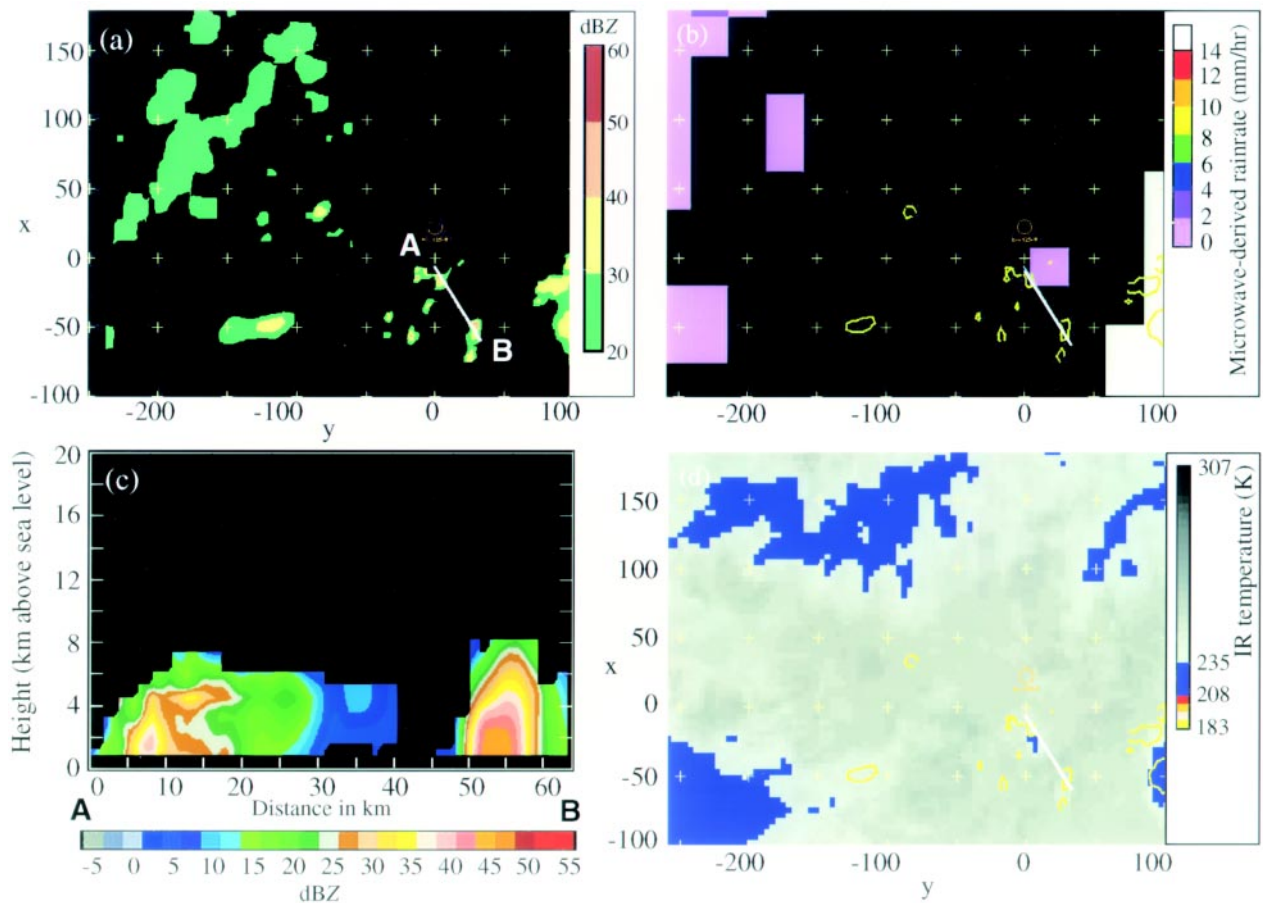


FIG. 14. Comparison of radar echo, IR temperature, and SSM/I derived precipitation. Data times are at 1600 UTC 11 Aug 1997 for GOES IR, 1550 UTC for SSM/I, and 1545 UTC for the radar data. (a) Radar reflectivity at ~ 0.5 km altitude in vicinity of ship position at $x = 0$, $y = 0$. (b) SSM/I-derived precipitation overlain with radar reflectivity contours at 30 dBZ. (c) Vertical cross section of radar reflectivity along line A–B indicated in (a). (d) GOES IR temperature data for same region overlain with radar reflectivity contours at 30 dBZ. The IR temperatures between 208 and 235 K are blue; IR temperatures < 208 K are red and orange. Vertical axis in (a) also applied to (b).

(GPI) methodology (Arkin and Meisner 1987) is based on an empirical relation between frequency of IR temperature < 235 K and rain rate derived over large areas ($2.5^\circ \times 2.5^\circ$) and long time periods (least 5 days) and is not applicable to small areas and instantaneous data. In this section, we use TEPPS data to relate more precisely the three-dimensional structure of storms to the expression of that structure in terms of IR cloud-top temperature and microwave-derived surface precipitation. We examine the spatial variability of precipitation derived from microwave data in relation to three-dimensional volumes of ship radar reflectivity. Qualitative comparison of satellite-precipitation estimates with three-dimensional reflectivity data tests a number of the physical assumptions of the satellite algorithms and can indicate direction of algorithm improvement.

Comparisons between the quality-controlled, interpolated radar data described in section 3b and microwave-derived precipitation estimates are made within the region of their overlap, which often covers only a portion of a large precipitating system. The minimum detectable radar reflectivity is a function of the radar characteristics and increases with increasing range. Minimum detectable reflectivity during the TEPPS cruise was 13 dBZ at 100-km range and 20 dBZ at 240-km range. In the absence of a Z – R relation (see section 3c), we make two simple assumptions about the relation between radar reflectivity and precipitation: near-surface radar reflectivities > 20 dBZ are produced by precipitation > 0.5 mm h^{-1} , and increasing reflectivity is associated with increasing rainfall rate. Two-dimensional maps of reflectivity at 4-km resolution derived from the low-level surveillance scans

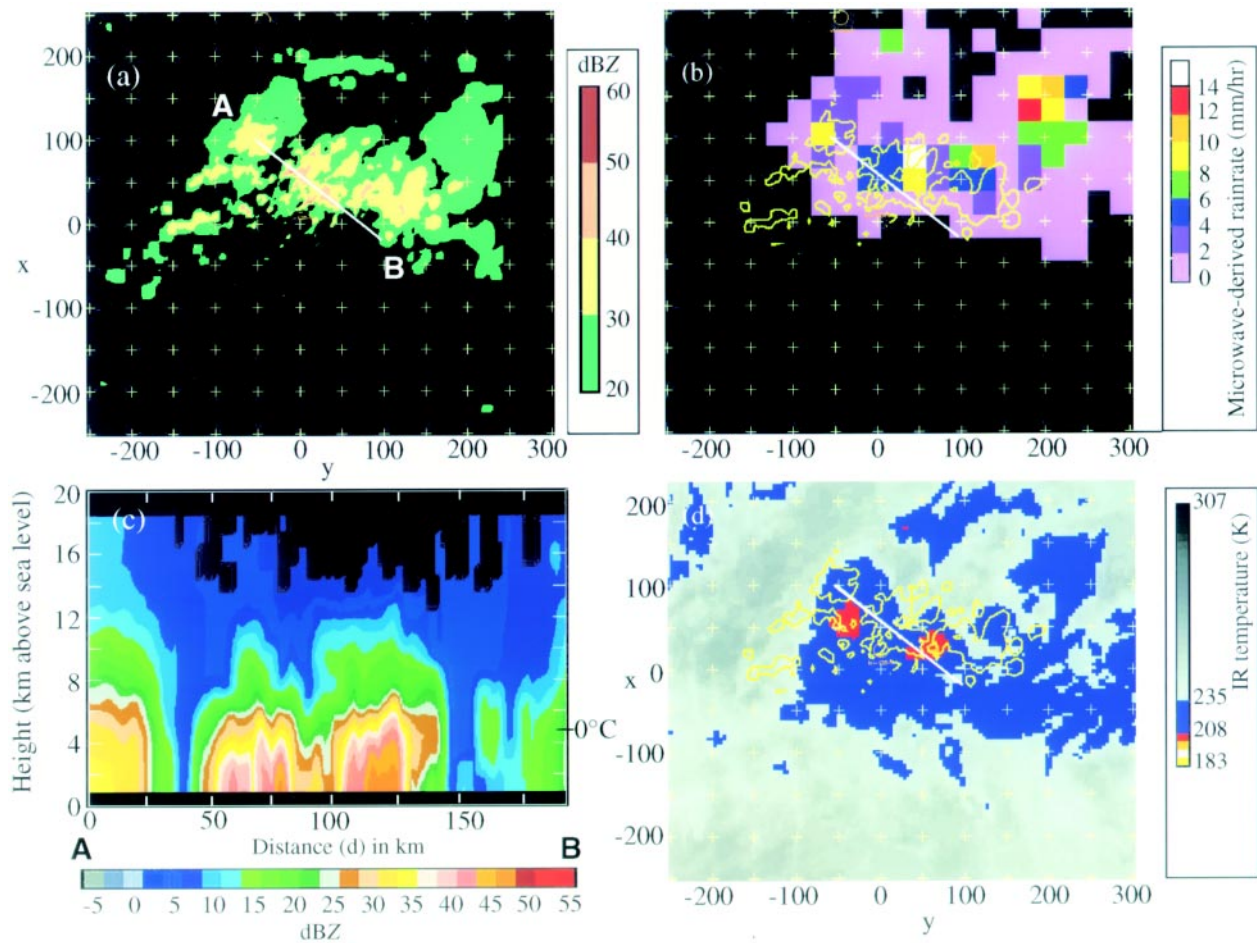


FIG. 15. Same as Fig. 14 except data times are 0300 UTC 11 Aug 1997 for GOES IR, 0312 UTC for SSM/I, and 0315 UTC for the radar data.

(section 3b) characterize the near-surface radar echoes out to 240 km from the ship. The three-dimensional radar data is of higher spatial resolution (section 3b) than the microwave data, and can indicate the presence of higher reflectivity convective cells with localized heavy rainfall and smaller precipitating features that are not resolved by the satellite data. The radar data can characterize details of the vertical hydrometeor distribution such as the location of the melting layer, the presence and depth of precipitation-sized ice layers, and whether precipitation is convective or stratiform. Errors in reflectivity due to attenuation⁵ are a

⁵C-band radar reflectivities at far ranges can be attenuated by heavy rainfall closer to the radar at a rate of ~ 0.003 dB/km/mm/hr (Battan 1973). A raining region 5 km wide with uniform 100 mm/h rain rate will attenuate the reflectivities behind it by ~ 1.5 dB.

concern when converting from reflectivity to rain rate since small errors in reflectivity can yield large differences in rainfall rate. However, for the purposes of the following qualitative comparisons, these errors are not significant. The footprint of the Defense Meteorological Satellite Program SSM/I sensor is a function of frequency and varies from 69×43 km² at 19.35 GHz to 15×13 km² at 85.5 GHz. The Ferriday–Avery SSM/I rain maps have a horizontal resolution of ~ 28 km. Microwave algorithms assume a homogeneous rain field within the pixel (Kummerow 1998). When a precipitating region is smaller than the sensor resolution, beam filling will reduce or may eliminate the signature of that feature in the coarser resolution data. There appears to be a small southerly offset (~ 10 km) between the ship radar and microwave data navigation, which may vary among orbits, but for the purposes of the following comparisons, this is not significant.

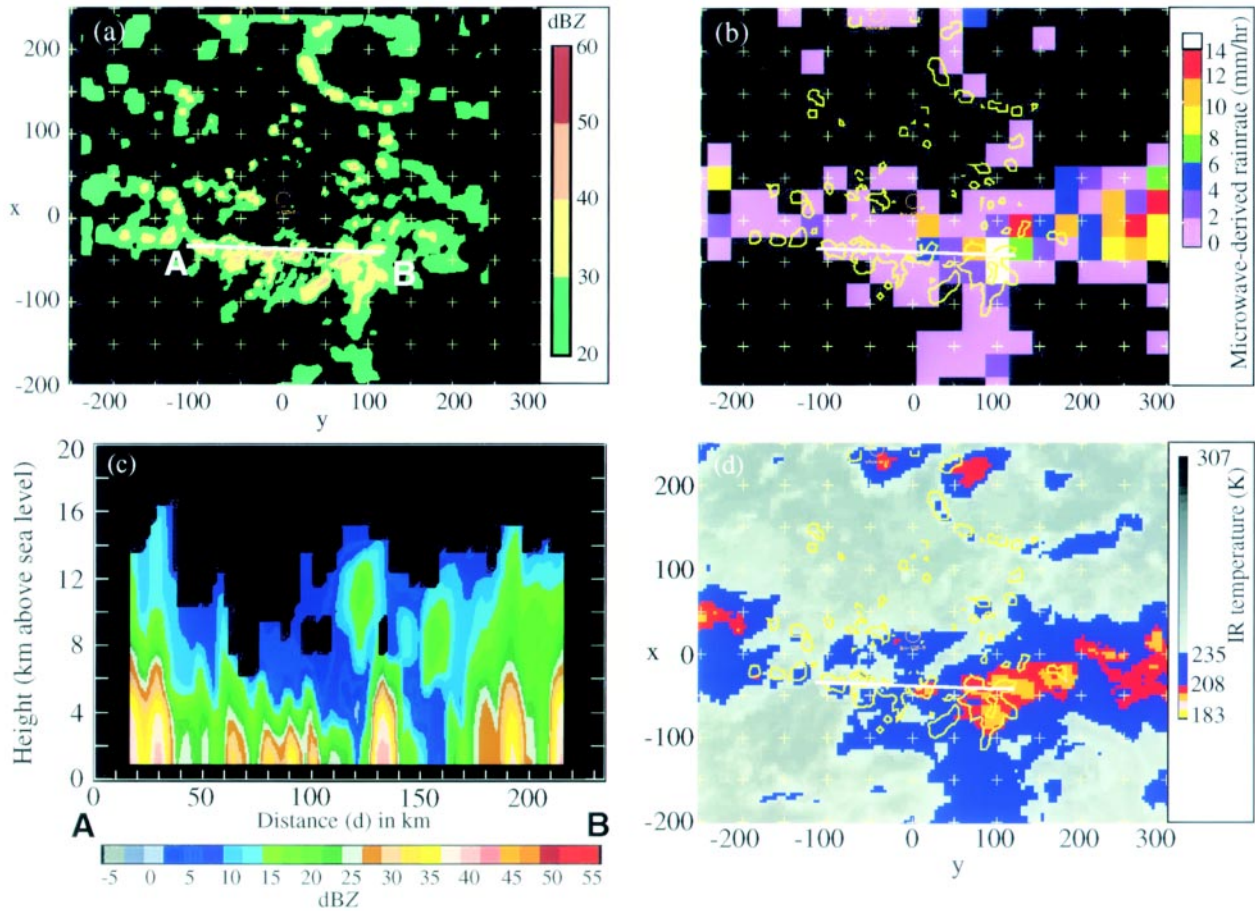


FIG. 16. Same as Fig. 14 except data times are 0500 10 Aug 1997 for GOES IR, 0455 UTC for SSM/I, and 0500 UTC for the radar data.

The higher-resolution radar data provide information on what types of precipitation structures are not resolved by the microwave-satellite precipitation algorithm. Figure 14 shows a set of isolated cells whose horizontal dimension was about 10 km. In the vertical cross section in Fig. 14c, it can be seen that both cells contained reflectivities > 40 dBZ and that they extend above the 0° level and contain ice, as evidenced by the enhancement of reflectivity associated with the brightband adjacent to the left-hand cell at a distance along the cross section (d) = 10–27 km. The cell on the right, which was not resolved in the microwave-derived precipitation field extended slightly higher (15-dBZ contour at 7 km) than the one on the left (15-dBZ contour at 6 km). In the 4-km resolution GOES IR data (Fig. 14d), only the cell on the left had cloud-top temperatures < 235 K. The colder cloud-top temperature and hence increased ice scattering associated with the cell on the left may have contributed to its being resolved in the microwave data. The echo

located at $x = -50$, $y = -125$ in Fig. 14a is also not detected in the microwave rain map (Fig. 14b). The contiguous region of radar echo > 20 dBZ is approximately 50 km in length and ~ 10 km wide. Examination of other simultaneous radar and microwave data (not shown) indicates that the radar echo needs to be larger than ~ 10 km in both long and short dimensions in order to be reliably detected in the Ferriday–Avery SSM/I instantaneous rain maps.

On 11 August 1997, a large region of precipitation with contiguous radar echoes > 100 km occurred within range of the ship radar. Figure 15 compares reflectivities from 0315 UTC with the microwave algorithm precipitation field from an overpass at 0312 UTC, and the GOES IR data from 0300 UTC. For the region where the radar reflectivity overlapped, the microwave precipitation data were in fairly good agreement regarding the size and shape of the precipitating region (edge of green area on radar data and edge of pink area on microwave data). The micro-

wave-derived precipitation field does not capture the elongated reflectivity feature to the southwest, but the general outline of precipitating versus nonprecipitating region matches fairly well.

Comparison of the pattern of relative rainfall rates indicated by the microwave algorithm and the radar reflectivity illustrates the complexity of their joint variation. The vertical cross section reveals a group of strong convective cells with near-surface reflectivities ~40–47 dBZ from $d = 55$ to 125 km with 15-dBZ contour heights of 7–10 km (Fig. 15c). The cell on the northwest end (A) of the cross section (0–25 km) had 15-dBZ echo to 11-km altitude and surface reflectivities near 35 dBZ. In this case, the microwave algorithm correctly indicates the location of the portions of the cross section with higher rain rates in comparison to the weaker background rainrate. However, the relative magnitudes of the precipitation associated with the northwest cell versus the group of cells in the center of the cross section are inconsistent with their near-surface reflectivities. The microwave algorithm associates a higher rain rate (8–10 mm h⁻¹) with the lower near-surface reflectivities (~35 dBZ) of the northwest cell and a lower rainrate (4–6 mm h⁻¹) with the higher near-surface reflectivity (40–47 dBZ) of the group of cells in the center. In this example, the radar data indicate that higher surface reflectivities, and hence rain rates, are associated with a shallower ice layer. The offset to the southwest of the < 235 K cloud tops from the > 30 dBZ radar echoes (up to 50 km; Figs. 15c,d) is likely associated with the displacement of high cloudiness from the surface rainfall rather than navigation error since the Doppler radial velocity data for this time period (not shown) indicate that winds at ~10 km altitude were southwesterly.

On 10 August 1997, another precipitating region with contiguous echoes > 100 km in scale was present in the vicinity of the ship. Figure 16b shows good correspondence in the size and shape of the precipitating region seen in the radar and microwave algorithm. The elongated reflectivity feature to the northeast was captured in the microwave data. The small navigation offset between the radar and microwave data is evident along the south edge of the feature. The vertical cross section through the radar data shows a line of cells with maximum reflectivities ~40 and 15 dBZ contour heights from 3- to 15-km altitude. Most of the cells in the vertical cross section have reflectivity cores > 35 dBZ. On the eastern end of the cross section where the microwave algorithm indicates higher rainfall rates, 15-dBZ contours extend to 15 km, while on the

central and western ends of the cross section, the 15-dBZ contours are lower (8–10 km). The near-surface reflectivities are higher on the western end of the cross section than the eastern end reversed from the microwave precipitation rate pattern. For example, the 40-dBZ cell at $d = 20$ km is grossly inconsistent with the 0–2 mm h⁻¹ rain rate in the microwave data. The higher microwave precipitation rates > 10 mm h⁻¹ at the eastern end of the cross section are more consistent with the spatial pattern of the depth of the ice layer as indicated by the colder cloud-top temperatures and the height of the 15-dBZ contour than the near-surface reflectivities. The presence of higher concentrations of ice aloft may trigger higher rain rates in the microwave algorithm.

In examining these and other examples of simultaneous radar and microwave data, the following trends are apparent. There is generally good agreement between radar and microwave data regarding the *size* and *shape* of precipitating regions larger than ~10 km in horizontal scale. However, within these larger precipitating regions, the degree of agreement between the *spatial pattern of higher rainfall rates* in the Ferriday–Avery microwave-derived precipitation estimate and higher radar reflectivities varies strongly. Previous studies examining coincident radar reflectivity and microwave-derived rainfall data have also indicated a variation in the degree of agreement between radar and microwave heavier rainfall areas (Liu and Curry 1992, their Fig. 21; Ferriday and Avery 1994, their Figs. 8–10; Kummerow and Giglio 1994, their Fig. 4). It is usually assumed that differences in the spatial location of heavier rainfall, although sometimes large for individual examples, will be small on average. However, this assumption has not been rigorously examined in algorithm intercomparison workshops to date since satellite precipitation algorithms are usually validated in terms of the areal average rainfall over regions $\geq 0.5^\circ$ (Ebert et al. 1996). If accurately locating the spots of heavier rainfall within rain areas is shown to be systematically problematic for microwave methods, areal average methods⁶ for estimating precipitation, such as are used with radar and IR data (Doneaud et al. 1981, 1984; Atlas et al. 1990; Arkin and Meisner 1987), may lead to better overall monthly rainfall estimates by using the microwave data to identify the

⁶Areal average methods use the remote sensor only to locate where precipitation is occurring and apply an empirical areal-average rain rate to that region.

raining area and applying an appropriate average precipitation rate.

6. Conclusions

A comprehensive set of observations of the structure of clouds and precipitating storms over the eastern tropical Pacific were obtained from the NOAA ship *Ronald H. Brown* during the 1997 PACS TEPPS cruise. Scanning C-band Doppler-radar data and cloud photography documented the nature of clouds and precipitation in the vicinity of the ship. Upper-air soundings were obtained at ≤ 4 h intervals and surface meteorological and oceanographic instruments and vertically pointing 915-MHz and S-band profilers characterized conditions at the ship itself.

The principal objective of the PACS TEPPS cruise was to understand the physical reasons behind the differences in the pattern of precipitation over the tropical eastern Pacific ITCZ derived from satellite IR versus microwave data (Janowiak et al. 1995; Fig. 2). Since both IR and microwave brightness temperatures are directly related to the vertical structure of precipitation and only indirectly related to rainfall, the observational focus of the project was an observation of the three-dimensional structure of radar reflectivity and Doppler velocity in order to address simultaneously the three-dimensional storm structure and the surface rainfall. In addition, the three-dimensional radar data provides contextual information that aids in subsetting the surface, upper-air sounding, and vertically pointing data into periods that are representative of synoptic conditions versus periods that are influenced by local convection. Within the time periods influenced by local convection, the radar data permit further subdivision of the ship-based data into storm inflow versus storm outflow subsets. These results illustrate the inherent difficulty in interpreting short timescale buoy data without benefit of the mesoscale context provided by radar data.

Observations made during the TEPPS cruise indicated a high frequency of occurrence of precipitating storms in the region of the eastern Pacific ITCZ near 8°N , 125°W during the on-station period in August 1997. Contiguous regions of precipitation with reflectivities > 20 dBZ that were larger than 50 km in scale occurred during $\sim 66\%$ of the hours on station. Precipitation regions larger than 100 km in scale occurred 49% of the time. During 41% of the daylight hours on station, cumulonimbus clouds were visually

observed within approximately ~ 100 km range of the ship. Rainfall was visually observed during the day within 50-km range of the ship 45% of the time. In contrast, rainfall was detected at the ship itself during only 17% of the hours on station. The longer-lived, larger-scale ($L \geq 100$ km) convective precipitation activity and organization was strongly associated with low-level southerly wind regimes (Fig. 11). This association is consistent with regulation by large-scale atmospheric processes such as easterly waves of inertial stability oscillations as have been proposed by Tomas and Webster (1997).

The TEPPS cruise data showed that IR cold cloudiness < 235 K reliably detected only the large (> 100 km scale), long-duration (> 24 h) precipitating regions, that is, the mesoscale organized convective systems (Figs. 11d, 12). Precipitating systems of shorter duration and/or smaller scale in the eastern Pacific ITCZ did not always produce cloud tops < 235 K. The radar-observed surface rain patterns showed that satellite microwave data yielded generally accurate areal coverage and location of precipitating regions larger than ~ 10 km in horizontal scale. Beam filling likely contributed to the SSM/I data failing to detect raining isolated cells and long, narrow precipitating echoes < 10 km in width. The microwave algorithm examined in this study (Ferriday and Avery 1994) exhibited varying degrees of skill in locating the heavier rainfall within the rainy regions.

The main contrast between IR and microwave data occurred during periods when IR high cloudiness < 235 K was absent. Radar data revealed these periods to be convectively active in terms of overturning of the atmosphere and precipitation formation but the precipitating regions were of smaller horizontal scale and/or shorter duration. Rather than indicating suppression of convection per se (i.e., little to no atmospheric overturning), absence of high cloudiness in the eastern Pacific ITCZ indicates periods when the tendency for precipitating systems to *organize* into large, long-lived mesoscale systems is reduced.

The comparison of TEPPS radar reflectivity data with satellite IR and microwave data contributes toward discerning whether the precipitation maximum in the Pacific is in the east or west. Part of the reason IR versus microwave-derived precipitation maps differ in the eastern Pacific is that the IR cold cloudiness resolves only a subset of the precipitation detected by microwave data. The contribution to overall rainfall by the smaller, less organized convection detected by microwave algorithms but not by IR cold cloudiness

is therefore key to revealing the true distribution of precipitation in the Pacific. The verification of the magnitude of precipitation in the eastern Pacific estimated by microwave algorithms will require comparison to forthcoming TEPPS rain maps.

The TEPPS dataset presents the opportunity for a wide variety of investigations related to eastern Pacific precipitation. Although TEPPS was shorter in duration and smaller in radar areal coverage than TOGA COARE and GATE, comparisons to data collected in those projects will bring to light the degree of variation in open ocean tropical precipitation across the Pacific basin and between the eastern Atlantic ITCZ and eastern Pacific ITCZ. We encourage other investigators to make use of the TEPPS dataset in their studies. Data from the TEPPS cruise can be obtained online at (www.atmos.washington.edu/gcg/MG/tepps/) and at (www.ucar.joss.edu/codiac/).

Acknowledgments. Greatly appreciated were the scientific comments, help, and advice of Steve Anderson, Christopher Bretherton, Marcia Baker, Dennis Engemoen, David Hosom, Warren Keenan, George Kiladis, Conway Leovy, Brian Mapes, Steve Piotrowicz, Yolande Serra, Todd Mitchell, and Robert Weller. Wesley Berg, Stacy Brodzik, Richard Pasch, and Joe Tenerelli supplied both the ship and the on shore operations in Seattle with a variety of model and satellite datasets during the cruise. Wesley Berg and Steve Williams provided additional satellite data for analysis after the completion of the cruise. Special thanks go to Grant Gray, the radar engineer responsible for installation and operation of the C-band radar on the *Brown* during TEPPS. Thanks to the TEPPS scientific crew: Bart Brashers, Matthew Carr, Martin Grossklaus, Mary Landahl, Brian Mapes, Courtney Schumacher, Catherine Spooner, Yolande Serra, and Christopher Williams; to the NOAA engineers and technicians who worked to get the ship ready on time for its scientific cruise; and to the officers and crew of the *Brown* under the command of Captain David Peterson for their exemplary support of the scientific mission. Candace Gudmundson edited the manuscript and Kay Dewar drafted some of the figures. Robert Beaufait, Ian Horton, Michele Kruegel, Wendy Parker, Katherine Pearl, and Catherine Spooner assisted in organizing and postprocessing the cruise data for analysis and distribution. Suggestions by three reviewers have contributed to improvement of the manuscript. This research was supported by NOAA Cooperative Agreement NA67RJO115 and NASA TRMM NAG5-4795.

Appendix A: Calibration and accuracy of surface time series sensors

The ASIMET sensors onboard (Hosom et al. 1995) the *Brown* during the TEPPS cruise were calibrated in April 1997 at WHOI. Systematic discrepancies be-

tween the ASIMET relative humidity measurements and relative humidity measured from hand-held sling psychrometers led to taking the temperature and relative humidity instruments off the ship at the conclusion of the cruise for a postcruise calibration. Corrections were derived for relative humidity amounting to a few percent and for temperature of $\sim 0.2^\circ\text{C}$ and were applied to the time series data collected during TEPPS. The air temperature sensor is also subject to radiative heating errors when relative wind speeds are low (Anderson and Baumgartner 1998). The non-ASIMET surface meteorology and upper-ocean instrumentation were calibrated by the manufacturers prior to deployment. Since the ship itself can perturb the atmosphere more than a buoy, measurement errors for the surface meteorological instruments are expected to be greater or similar to those on a WHOI IMET buoy (Table A1; Weller and Anderson 1996).

Upon completion of the cruise, the seawater intakes were removed for cleaning and a small mullosk was found to be living inside. It is unknown when the mullosk moved in, so contributions to measurement error from biofouling have to be assumed for the entire cruise.

Appendix B: Detailed description of profiler operations

The NOAA Aeronomy Laboratory profilers collected data at several vertical resolutions correspond-

TABLE A1. Estimated accuracies of TEPPS surface meteorological instruments based on analysis from Weller and Anderson (1996) for WHOI IMET buoy deployments. The surface meteorological time series data are also used for the first upper-air sounding data point. Most of the surface meteorological instruments on the ship were provided by WHOI and are of similar type and underwent similar calibration to instruments used in WHOI buoy deployments.

Parameter	Instantaneous accuracy	Units
Wind speed	5	%
Wind direction	10	deg
Barometric pressure	0.5	hPa
Air temperature	0.2	$^\circ\text{C}$
Relative humidity	4	%

TABLE B1. Selected characteristics of NOAA Aeronomy Laboratory profilers associated with each pulse length mode.

	915 MHz			S band		
	60	105	495	60	105	495
Pulse length (m)	60	105	495	60	105	495
Gate spacing (m)	60	105	315	60	105	315
Altitude of first gate (m)	54	105	198	43	92	198
Altitude of last gate (m)	3800	6700	18 900	3 800	6 700	18 900
Min detectable signal (4 km)	6.9	2.3	-11.4	-10.3	-14.9	-28.6
Max detectable signal (4 km)	67.5	62.9	49.2	52.1	47.5	33.8
Regime when employed	Sc	ITCZ/Sc	ITCZ	Sc	ITCZ/Sc	ITCZ

ing to different pulse lengths (Table B1). For a given pulse length, the vertical profile of horizontal winds was sampled every 3 min by the 915-MHz profiler using one vertically pointing beam and two 69° elevation angle beams 90° apart in azimuth. Individual beam dwell times were 30 s for all pulse length modes and pointing directions. These samples were combined over a 25-min period to produce a consensus horizontal wind profile. During nonprecipitating periods, the profile of horizontal wind typically extended from the surface to 3–4-km altitude. During precipitation events, the increased depth of scatterers allowed the profiler to resolve horizontal winds to higher altitudes. For 5 min every half hour, RASS measurements were made with the 915-MHz profiler pointed vertically and four surrounding acoustic speakers activated to derive vertical profiles of virtual temperature. RASS data were typically available to 700-m altitude in nonprecipitating situations. RASS measurements are compromised in precipitation since the detected vertical air motion, which is used in the derivation of virtual temperature, includes a contribution from hydrometeor fall speeds that is difficult to remove (Parsons et al. 1994).

References

Adler, R. F., M. J. Markus, D. D. Fenn, G. Szejwach, and W. Shenk, 1983: Thunderstorm top structure observed by aircraft overflights with an infrared radiometer. *J. Climate Appl. Meteor.*, **22**, 579–593.

- Anderson, S. P., and M. F. Baumgartner, 1998: Radiative heating errors in naturally ventilated air temperature measurements made from buoys. *J. Oceanic. Atmos. Technol.*, **15**, 157–173.
- , R. A. Weller, and R. B. Lucas, 1996: Surface buoyancy forcing and the mixed layer of the western Pacific warm pool: Observations and 1D model results. *J. Climate*, **9**, 3056–3085.
- Arkin, P. A., and B. M. Meisner, 1987: The relationship between large-scale convective rainfall and cold cloud over the western hemisphere during 1982–84. *Mon. Wea. Rev.*, **115**, 51–74.
- Atlas, D., D. Rosenfeld, and D. A. Short, 1990: The estimation of convective rainfall by area integrals. Part I: The theoretical and empirical basis. *J. Geophys. Res.*, **95**, 2153–2160.
- Austin, P. M., and S. G. Geotis, 1980: Precipitation measurements over the ocean. *Air–Sea Interaction*, F. Dobson, L. Hasse, and R. Davis Eds., Plenum Publishing, 523–541.
- Barrett, E. C., and C. K. Grant, 1979: Relations between frequency distributions of cloud over the United Kingdom based on conventional observations and imagery from LANDSAT 2. *Weather*, **34**, 416–424.
- Battan, L. J., 1973: *Radar Observations of the Atmosphere*. University of Chicago Press, 324 pp.
- Burpee, R. W., 1975: Some features of synoptic-scale waves based on compositing analysis of GATE data. *Mon. Wea. Rev.*, **103**, 921–925.
- , and R. J. Reed, 1982: Synoptic-scale motions. *GARP Atlantic Tropical Experiment (GATE) Monogr.*, No. 25, GARP Publication Series, 61–113.
- Carter, D. A., W. L. Ecklund, K. S. Gage, M. Spowart, H. L. Cole, E. F. Chamberlain, W. F. Dabbert, and J. Wilson, 1992: First test of a shipboard wind profiler. *Bull. Amer. Meteor. Soc.*, **73**, 1587–1592.
- , K. S. Gage, W. L. Ecklund, W. M. Angevine, P. E. Johnston, A. C. Riddle, J. Wilson, and C. R. Williams, 1995: Developments in UHF lower tropospheric wind profiling at NOAA’s Aeronomy Laboratory. *Radio Sci.*, **30**, 977–1001.

- Chen, S. S., R. A. Houze Jr., and B. E. Mapes, 1996: Multiscale variability of deep convection in relation to large-scale circulation in TOGA COARE. *J. Atmos. Sci.*, **53**, 1380–1409.
- Doneaud, A. A., P. L. Smith, A. S. Dennis, and S. Sengupta, 1981: A simple method for estimating convective rain volume over an area. *Water Resour. Res.*, **17**, 1676–1682.
- , S. I. Niscov, D. L. Preignitz, and P. L. Smith, 1984: The area–time integral as an indicator for convective rain volumes. *J. Climate Appl. Meteor.*, **23**, 555–561.
- Ebert, E. E., M. J. Manton, P. A. Arkin, R. J. Allam, G. E. Holpin, and A. Gruber, 1996: Results from the GPCP Algorithm Intercomparison Programme. *Bull. Amer. Meteor. Soc.*, **77**, 2875–2887.
- Ecklund, W. L., P. E. Johnston, J. M. Warnock, W. L. Clark, and K. S. Gage, 1995: An S-band profiler for tropical precipitating cloud studies. Preprints, *27th Conf. on Radar Meteorology*, Vail, CO, Amer. Meteor. Soc., 335–336.
- Ferriday, J. G., and S. K. Avery, 1994: Passive microwave remote sensing of rainfall with SSM/I: Algorithm development and implementation. *J. Appl. Meteor.*, **33**, 1587–1596.
- Gage, K. S., C. R. Williams, and W. L. Ecklund, 1994: UHF wind profilers: A new tool for diagnosing tropical convective cloud systems. *Bull. Amer. Meteor. Soc.*, **75**, 2289–2294.
- , —, and —, 1996: Application of the 915-MHz profiler for diagnosing and classifying tropical precipitating cloud systems. *Meteor. Atmos. Phys.*, **59**, 141–151.
- Godfrey, J. S., R. A. Houze Jr., R. H. Johnson, R. Lukas, J.-L. Redelsperger, A. Sumi, and R. Weller, 1998: COARE: An interim report. *J. Geophys. Res.*, **103** (C7), 14 395–14 450.
- Grossklau, M., K. Uhlig, and L. Hasse, 1998: An optical disdrometer for use in high wind speeds. *J. Atmos. Oceanic Technol.*, **15**, 1051–1059.
- Hartten, L. M., 1998: Reconciliation of surface and profiler winds at ISS sites. *J. Oceanic Atmos. Technol.*, **15**, 826–834.
- Hasse, L., M. Grossklau, K. Uhlig, and P. Timm, 1998: A ship rain gauge for use in high wind speeds. *J. Atmos. Oceanic Technol.*, **15**, 380–386.
- Hayes, S. P., L. J. Mangum, J. Picaut, A. Sumi, and K. Takeuchi, 1991: TOGA-TAO: A moored array for real-time measurements in the tropical Pacific Ocean. *Bull. Amer. Meteor. Soc.*, **72**, 339–347.
- Heymsfield, G. M., and R. Fulton, 1988: Comparison of high-altitude remote aircraft measurements with radar structure of an Oklahoma thunderstorm: Implications for precipitation estimation from space. *Mon. Wea. Rev.*, **116**, 1157–1174.
- Hosom, D., R. A. Weller, R. E. Payne, and K. E. Prada, 1995: The IMET (Improved Meteorology) ship and buoy systems. *J. Atmos. Oceanic Technol.*, **12**, 527–540.
- Hudlow, M. D., 1979: Mean rainfall patterns for the three phases of GATE. *J. Appl. Meteor.*, **18**, 1656–1669.
- Janowiak, J. E., P. A. Arkin, P. Xie, M. L. Morrissey, and D. R. Legates, 1995: An examination of the east Pacific ITCZ rainfall distribution. *J. Climate*, **8**, 2810–2823.
- Joss, J., and A. Waldvogel, 1967: Ein Spektrograph für Niederschlagstropfen mit automatischer Auswertung. *Pure Appl. Geophys.* **68**, 240–246.
- Kuettner, J. P., D. E. Parker, D. R. Rodenhuis, H. Hofer, H. Kraus, and G. Philander, 1974: GATE final international scientific plans. *Bull. Amer. Meteor. Soc.*, **55**, 711–744.
- Kummerow, C., 1998: Beamfilling errors in passive microwave rainfall retrievals. *J. Appl. Meteor.*, **37**, 356–370.
- , and L. Giglio, 1994: A passive microwave technique for estimating rainfall and vertical structure information from space. Part II: Applications to SSM/I data. *J. Appl. Meteor.*, **33**, 19–34.
- Lin, X., and R. H. Johnson, 1996: Heating, moistening, and rainfall over the western Pacific warm pool during TOGA COARE. *J. Atmos. Sci.*, **53**, 3367–3383.
- Liu, G., and J. A. Curry, 1992: Retrieval of precipitation from satellite microwave measurement using both emission and scattering. *J. Geophys. Res.*, **97**, 9959–9974.
- Loehrer, S. M., T. A. Edmands, and J. A. Moore, 1996: TOGA COARE upper-air sounding data archive: Development and quality control procedures. *Bull. Amer. Meteor. Soc.*, **77**, 2651–2671.
- Machado, L. A. T., W. B. Rossow, R. L. Guedes, and A. W. Walker, 1998: Life cycle variations of mesoscale convective systems over the Americas. *Mon. Wea. Rev.*, **126**, 1630–1654.
- McCartney, E. J., 1976: *Optics of the Atmosphere Scattering by Molecules and Particles*. John Wiley and Sons, 408 pp.
- Mitchell, T. P., and J. M. Wallace, 1992: The annual cycle in equatorial convection and sea surface temperature. *J. Climate*, **5**, 1140–1156.
- Nystuen, J. A., 1999: Relative performance of automatic rain gauges under different rainfall conditions. *J. Atmos. Oceanic Technol.*, **16**, 1025–1043.
- , J. R. Proni, C. A. Lauter Jr., J. Bufkin, U. Rivero, M. Borland, and J. Wilkerson, 1994: APL disdrometer evaluation. NOAA Tech. Memo. ERL AOML-83, Atlantic Oceanographic and Meteorological Laboratory, Miami, FL, 43 pp. [Available from National Technical Information Service, 5285 Port Royal Road, Springfield, VA 22161.]
- Parsons, D., and Coauthors, 1994: The integrated sounding system: description and preliminary observations from TOGA COARE. *Bull. Amer. Meteor. Soc.*, **75**, 553–567.
- Reed, R. J., and E. E. Recker, 1971: Structure and properties of synoptic-scale wave disturbances in the equatorial western Pacific. *J. Atmos. Sci.*, **28**, 1117–1133.
- Rinehart, R. E., 1995: Student-determined Z–R relationship for North Dakota using filter paper technique. Preprints, *27th Conf. on Radar Meteorology*, Vail, CO, Amer. Meteor. Soc., 58–60.
- Short, D. A., P. A. Kucera, B. S. Ferrier, J. C. Gerlach, S. A. Rutledge, and O. W. Thiele, 1997: Shipboard radar rainfall patterns within the TOGA COARE IFA. *Bull. Amer. Meteor. Soc.*, **78**, 2817–2836.
- Skaar, J., 1955: On the measurement of precipitation at sea. *Geofysiske Publikasjoner*, Vol. XIX, No. 6, Utgitt av Det Norske Videnskaps-Akademi i Oslo, 32 pp.
- Smith, E. A., A. Mugnai, H. J. Cooper, G. J. Tripoli, and X. Xiang, 1992: Foundations for statistical-physical precipitation retrieval from passive microwave satellite measurements. Part I: Brightness-temperature properties of a time-dependent cloud radiation model. *J. Appl. Meteor.*, **31**, 506–531.
- , and Coauthors, 1998: Results of the WetNet PIP-2 project. *J. Atmos. Sci.*, **55**, 1483–1536.
- Spencer, R. W., 1993: Global oceanic precipitation from the MSU during 1979–91 and comparison to other climatologies. *J. Climate*, **6**, 1301–1326.

- Tomas, R. A., and P. J. Webster, 1997: The role of inertial instability in determining the location and strength of near equatorial convection. *Quart. Roy. Meteor. Soc.*, **123**, 1445–1482.
- Wang, T., K. B. Earnshaw, and R. S. Lawrence, 1979: Path-averaged measurements of rain rate and raindrop size distribution using a fast-response optical sensor. *J. Appl. Meteor.*, **18**, 654–660.
- Wanninkhof, R., H. B. Milburn, C. E. Cosca, M. Stapp, and P. P. Murphy, 1998: A new automated underway system for making high precision pCO₂ measurements onboard research ships. *Analytica Chim. Acta.*, **377**, 185–191.
- Warren, S. G., C. J. Hahn, J. London, R. M. Chervin, and R. L. Jenne, 1988: Global distribution of total cloud cover and cloud type amounts over ocean. NCAR Tech. Note NCAR/TN-37 + STR, National Center for Atmospheric Research, Boulder, CO, 42 pp. plus 170 maps. [Available from National Center of Atmospheric Research, P.O. Box 3000, Boulder, CO 80307.]
- Webster, P. J., and R. Lukas, 1992: TOGA COARE: The Coupled Ocean–Atmosphere Response Experiment. *Bull. Amer. Meteor. Soc.*, **73**, 1377–1416.
- Weller, R. A., and S. P. Anderson, 1996: Surface meteorology and air–sea fluxes in the western equatorial Pacific warm pool during the TOGA Coupled Ocean–Atmosphere Response Experiment. *J. Climate*, **9**, 1959–1990.
- Wilheit, T. T., 1986: Some comments on passive microwave measurement of rain. *Bull. Amer. Meteor. Soc.*, **67**, 1226–1232.
- Williams, C. R., W. L. Ecklund, and K. S. Gage, 1995: Classification of precipitating clouds in the tropics using 915-MHz wind profilers. *J. Atmos. Oceanic Technol.*, **12**, 996–1012.
- WMO, 1975: *International Cloud Atlas*. Vol. 1, *Manual on the Observation of Clouds and Other Meteors*, WMO, 155 pp. [Available from WMO, 7 bis A. de la Paix, CP2300-1211, Geneva 2, Switzerland.]
- Xie, P. and P. A. Arkin, 1996: Analyses of global monthly precipitation using gauge observations, satellite estimates, and numerical model predictions. *J. Climate*, **9**, 840–858.
- Yuter, S. E., and R. A. Houze Jr., 1998: The natural variability of precipitating clouds over the western Pacific warm pool. *Quart. J. Roy. Meteor. Soc.*, **124**, 53–99.

